



Deciphering the Pre-solar-storm Features of the 2017 September Storm From Global and Local Dynamics

Breno Raphaldini¹ , Mausumi Dikpati¹ , Aimee A. Norton² , Andre S. W. Teruya³ , Scott W. McIntosh¹ ,
Christopher B. Prior⁴ , and David MacTaggart⁵

¹ High Altitude Observatory, NCAR, 3080 Center Green Drive, Boulder, CO 80301, USA

² Hansen Experimental Physics Laboratory, 452 Lomita Mall, Stanford, CA 94305-4085, USA

³ Instituto de Astronomia, Geofísica e Ciências Atmosféricas, Universidade de São Paulo, São Paulo, Brazil

⁴ Department of Mathematical Sciences, Durham University, Stockton Road, Durham DH1 3LE, UK

⁵ School of Mathematics and Statistics, University of Glasgow, Glasgow G12 8QQ, UK

Received 2023 June 29; revised 2023 September 21; accepted 2023 September 26; published 2023 November 23

Abstract

We investigate whether global toroid patterns and the local magnetic field topology of solar active region (AR) 12673 together can hindcast the occurrence of the biggest X-flares of solar cycle (SC)-24. Magnetic toroid patterns (narrow latitude belts warped in longitude, in which ARs are tightly bound) derived from the surface distributions of ARs, prior and during AR 12673 emergence, reveal that the portions of the south toroid containing AR 12673 was not tipped away from its north-toroid counterpart at that longitude, unlike the 2003 Halloween storms scenario. During the minimum phase there were too few emergences to determine multimode longitudinal toroid patterns. A new emergence within AR 12673 produced a complex nonpotential structure, which led to the rapid buildup of helicity and winding that triggered the biggest X-flare of SC-24, suggesting that this minimum-phase storm can be anticipated several hours before its occurrence. However, global patterns and local dynamics for a peak-phase storm, such as that from AR 11263, behaved like the 2003 Halloween storms, producing the third biggest X-flare of SC-24. AR 11263 was present at the longitude where the north and south toroids tipped away from each other. While global toroid patterns indicate that prestorm features can be forecast with a lead time of a few months, their application to observational data can be complicated by complex interactions with turbulent flows. Complex nonpotential field structure development hours before the storm are necessary for short-term prediction. We infer that minimum-phase storms cannot be forecast accurately more than a few hours ahead, while flare-prone ARs in the peak phase may be anticipated much earlier, possibly months ahead from global toroid patterns.

Unified Astronomy Thesaurus concepts: [Solar activity \(1475\)](#); [Solar flares \(1496\)](#); [Solar storm \(1526\)](#); [Solar ARs \(1974\)](#)

Supporting material: animations

1. Introduction

Understanding and ultimately predicting intense explosive events such as large flares and coronal mass ejection (CME) events are currently the cornerstones of solar research due to their socioeconomic and environmental impacts (Simpson 2011; Khodairy et al. 2020; Vanselow 2020). One approach that has been explored in order to understand the circumstances that lead to large flares and CMEs is to study local physical properties in the vicinity of active regions (ARs) such as magnetic fluxes (Metcalf et al. 2005; Regnier & Priest 2007; Jing et al. 2010), plasma velocity fields (Attié et al. 2018), magnetic helicity (Pariat et al. 2005; Démoulin & Pariat 2009; Gupta et al. 2021), magnetic winding (MacTaggart et al. 2021; Raphaldini et al. 2022), and magnetic twist (Kusano et al. 2020). The evaluation of the predictive skill of several quantities and their potential operational applications can be found in a series of papers (Barnes et al. 2016; Leka et al. 2019a, 2019b; Park et al. 2020). Studies of plasma flows in flux emergence simulations on the other hand show that it is possible to predict new emergences within 10 hr of advance

(Silva et al. 2023). On the other hand, the global pattern of the toroid, the strong reservoir of magnetic field stored at depth in the Sun and from which ARs emerge, can provide certain features indicative of the occurrence of big solar storms (Dikpati et al. 2021).

The spatiotemporal organization of solar ARs follow well-known patterns both in latitude and longitude. Latitudinal migration is exemplified by the so-called butterfly diagram, from midlatitudes ($\sim 35^\circ$ – 30°) toward the equatorial region as the solar cycle (SC) progresses (Hathaway 2015). The butterfly diagram is understood in terms of the migration of toroidal magnetic field bands following the dynamo cycle and has been simulated using various dynamo models (Rüdiger & Brandenburg 1995; Dikpati & Gilman 2009; Cameron et al. 2017). Less obvious is the organization of ARs in longitude, namely the activity nests and long-lived preferred longitudes that can persist for long times, possibly beyond one SC (Balthasar & Schüssler 1983; Neugebauer et al. 2000). After the discovery of solar Rossby waves from observations (McIntosh et al. 2017; Löptien et al. 2018), preferred longitudes, where solar AR manifestations recur, have been explored by simulating interactions among Rossby waves, differential rotation, and toroidal magnetic fields. The tachocline is a likely region for these nonlinear interactions to take place, and sustained bulging at certain latitude–longitude locations are favorable for flux

emergence and can plausibly be the cause of AR nesting (Dikpati & McIntosh 2020).

Rossby waves are large-scale propagating patterns of vertical vorticity long known to exist in Earth’s atmosphere and oceans (Rossby 1939; Madden 1979), and are one of the key physical mechanisms for understanding global weather and climate dynamics (Hoskins & Valdes 1990; Hoskins & Ambrizzi 1993; Hoskins & Hodges 2002). While Rossby waves have long been hypothesized to exist in the Sun (Gilman 1968), the relationship between the dynamics of Rossby waves, modified by the presence of magnetic fields, and the longitude-dependent magnetic activity of the Sun was explored only recently (Dikpati & McIntosh 2020).

Rossby waves in the Sun, from observations and theory, can be classified to two distinct groups, namely those that are dynamic, and hence can shape the magnetic fields and patterns, and those that are of diagnostic value but for which individual modes are too low in amplitude to have an influence on magnetic patterns. The dynamic ones are of relatively low longitudinal wavenumber ($m = 1, 2,$ and 3) and there are only a few modes, each of which has a significant amplitude. These are mostly generated from global MHD instabilities (Dziembowski & Kosovichev 1987; Gilman & Fox 1997; Zaqarashvili et al. 2010a; Raphaldini & Raupp 2015; Dikpati et al. 2018a). Their signatures are observed in the solar magnetic patterns at the solar surface, in the spatial distribution of ARs (Dikpati et al. 2021), and at the corona, in the evolution of bright point densities (McIntosh et al. 2017) and in the longitude drift of long-lived coronal holes (Harris et al. 2022). It is to be noted that there can be other Rossby waves which can interact with mean magnetic fields. However, the Rossby waves that can interact locally with the dynamo-generated toroidal magnetic fields have to be located at/near the base of the convection zone.

Korsós et al. (2023) provided evidence for the link between intermediate periods, associated with meridional oscillations of photospheric structures, and the occurrence of large flares, suggesting that magnetic Rossby waves play a major role in the occurrence of these events. By contrast, helioseismically determined Rossby waves are numerous (Löptien et al. 2018) and each mode has a low amplitude. They include other inertial oscillations too (Hathaway et al. 2022). These Rossby waves can be understood from simulations also near the surface via the inverse cascade of kinetic energy, such as horizontal supergranular motions (Dikpati et al. 2022). Most recently, theory has shown the possible existence of thermal Rossby waves, whose properties are tied to the outward density decline in the convection zone coupled with rotation and differential rotation (Hindman & Jain 2022). They are yet to be observed. As more becomes known about this class of Rossby waves, the concept presented in this paper may need modification. But at the present time, to understand the pre-solar-storm properties from global magnetic patterns, we focus on the Rossby waves generated by global MHD instabilities, and elaborate on that in the following paragraph.

Studying properties such as characteristic frequencies and growth rates, (Zaqarashvili et al. 2010a, 2010b) suggested that magnetized Rossby waves in the solar tachocline were plausible sources for intermediate frequencies of solar magnetic activity (from several months up to a few years) such as Rieger-type periodicities and quasi-biennial oscillations. Using a nonlinear MHD shallow-water model, Dikpati et al. (2018a)

showed that there is a good match between the characteristic phase speed of magnetized Rossby waves and the longitudinal migration of magnetic field structures observed in the photosphere. Dikpati et al. (2017, 2018b) also showed, within the same framework, that an oscillatory exchange of energies among Rossby waves, differential rotation, and magnetic fields gives rise to so-called tachocline nonlinear oscillations (TNOs), which can explain bursty “seasons” of solar activity at intermediate timescales of a few weeks to several months. A similar type of nonlinear interaction between Rossby waves and zonal structures has also been invoked as a mechanism for longer-term periodicities of the Sun including the occurrence of grand minima (Raphaldini & Raupp 2015; Raphaldini et al. 2019, 2020).

Because the subject of solar Rossby waves is relatively new, at this point it is worthwhile to discuss analogies between the roles played by atmospheric Rossby waves on weather and climate and that played by solar Rossby waves on the magnetic activity of the Sun. It is well established that atmospheric Rossby waves constitute a mechanism that organizes weather patterns on large scales. One example is the so-called teleconnection patterns, consisting of geographically widely separated areas that have connected weather oscillations (Hoskins & Valdes 1990), such as observed in rainfall time series (Boers 2019). The link between Rossby waves and global rainfall patterns lie in the mechanisms of cloud formation and their relationship with low/high-pressure regions due to Rossby waves. Solar Rossby waves in the tachocline are also expected to generate sequences of high- and low-pressure regions in the formation of bulges at the top of the tachocline (Dikpati et al. 2018a). These bulging patterns will determine the locations from which magnetic fields will emerge through the convection zone, eventually reaching the photosphere and giving rise to ARs.

The association between atmospheric Rossby waves and weather systems was introduced by Sutcliffe (1947) and resulted in a substantial advance in the weather prediction practices before the era of supercomputing. Monitoring Rossby wave troughs and ridges (high/low-pressure regions) became an operational practice that expanded the prediction horizon from a few hours to several days compared with purely local observations of the cloud conditions (Bluestein 1992). With this solar-terrestrial weather analogy in mind, can monitoring solar Rossby waves extend the prediction horizon from a few hours to several days/weeks compared with pure observations of ARs’ physical properties?

Having discussed the important roles a class of solar Rossby waves play in organizing longitude distribution of ARs (see also Teruya et al. 2022; Raphaldini et al. 2023), analogous to the way atmospheric Rossby waves play for terrestrial weather patterns, we explore prestorm feature analysis from solar Rossby wave dynamics. Dikpati et al. (2021) derived toroid patterns by fitting low-order longitudinal modes to synoptic magnetogram maps. When applied to a prestorm configuration, namely the “Halloween Storms” of 2003, which originated from an X-45 class flare (Thomson et al. 2004), the wavy toroid patterns in the northern and southern hemispheres were found to tip away from each other at certain longitudes, and consequently at certain other longitudes the north and south toroids were found to come closer to each other. It was argued that the “tipped-away” portions of the toroids at a specific longitude led to big storms, first from the south and then in 2–3

days later from the north. The results were interpreted in terms of bulging generated by shallow-water Rossby waves and their perturbations to the toroidal magnetic field at the solar tachocline. Those simulations showed how fluid bulge movement from the south to the north in a couple of days can create “imprints” of big spot emergences from the same longitude in both hemispheres in the interval of a few days.

Big storms of similar strength to the Halloween storms did not occur in cycle 24, which was the weakest cycle in 100 yr. Instead, the biggest storm occurred on 2017 September 6, which was essentially in the minimum phase of that cycle. We seek to answer the following questions in this study: (i) can the global toroid patterns be derived for a storm that occurred during the minimum phase of a cycle, when there are very few spots? (ii) What can be inferred about the prestorm features in 2017 from those toroids? (iii) Even though rare, if the storms occur in a solar-minimum phase, and hence the global patterns may lack prestorm features from which to make forecasts, what can be inferred instead from local dynamics of the relevant ARs, in this case AR 12673? (iv) What are the differences in prestorm features derived from global and local patterns when the storms occur in a maximum phase compared to a minimum phase?

If global toroid patterns can indicate prestorm features, a lead time of a few weeks can be available to prepare for the prevention of hazardous space weather impacts. However, global toroid patterns cannot be very meaningfully constructed when there is only one spot, such as that often happens during very late declining phase of a cycle or during solar minimum. In those cases, if a big X-class flare occurs, local dynamics would be the only option to derive the prestorm features, but we lose the weeks-longer lead time because the indication from local dynamics provides only several hours lead time. It is clear that to utilize the predictive capability of models that can provide prestorm features best, we need to study both the global patterns of relevant ARs with a few weeks lead time as well as their local dynamics with a few hours lead time. In the present paper, we aim to study the connection between large-scale deformation patterns observed in the latitude–longitude organization of ARs observed from magnetic field synoptic maps, and the complexity of the ARs that led to the two largest flares during SC-24. The manuscript is organized as follows: in Section 2 we describe the methods used, including (i) an analysis of global magnetic field patterns through toroid fitting and (ii) a local analysis via topological characterizations of ARs via magnetic helicity and magnetic winding analyses. In Section 3 we describe the results from the global and local analyses both for an off-maximum storm (AR 12673) and for an AR in the solar maximum (AR 11263) which is also compared with an adjacent nonflaring region (AR 11266). Section 4 gives a summary, and Section 5 presents conclusions with an accompanying discussion.

2. Methods

As discussed in Section 1, we explore the pre–solar-storm features from global and local dynamics, to understand how far ahead in time the occurrence of a storm can be estimated. We discuss briefly in Section 2.1 the methodology for deriving the evolution of the global toroid, from which surface ARs manifest, by implementing the “Trust Region Reflective” (TRR) algorithm (see, e.g., Dikpati et al. 2021 for details). In Section 2.2 we describe the procedure for calculating helicity

and winding patterns for the ARs of our interest (see Raphaldini et al. 2022). We select AR 12673, which caused the biggest X-class flare of cycle 24 during 2017 September. Noting that the biggest X-flare occurred in the late declining phase of cycle 24, almost during the minimum phase, we also select another AR, AR 11263, which caused another big X-class flare during 2011, during the late rising phase just before the peak of cycle 24. Thus we can compare how the global and local dynamics can be indicative of prestorm properties at solar-minimum and maximum phases.

2.1. Deriving the Toroid Patterns of AR Distributions

Here we follow the formulation introduced in detail in Dikpati et al. (2021) for fitting toroid patterns to magnetic field synoptic maps. In the present study we use Helioseismic and Magnetic Imager (HMI) synoptic maps, which are constructed by combining near central meridian data from 20 magnetograms, resulting in 1440×3600 grid points of $\sin(\text{latitude}) \times \text{longitude}$ charts. These maps provide a representation of the latitudinal distribution of ARs as well as their Carrington longitude positions. The main idea introduced in Dikpati et al. (2021) is to represent the spatial distribution of ARs in terms of two wavy belts or toroids, one for each hemisphere, constructed by the superposition of Fourier modes. Given a synoptic chart at time t , global toroid patterns $P_c(\phi, t)$ are determined via the superposition of Fourier modes of the form:

$$P_c(\phi, t) = \sum_{m=0}^N q_m(t) \sin(m\phi + \zeta_m(t)). \quad (1)$$

Here $q_m(t)$ is the Fourier amplitude of the m th mode at time t and $\zeta_m(t)$ the respective Fourier phase. Both the Fourier amplitude and phases are represented as a combination of mean and time-varying parts:

$$q_m(t) = \bar{q}_m + \sum_i s_{i,m}(t_i), \quad (2)$$

$$\zeta_m(t) = \bar{\zeta}_m + \sum_i w_{i,m}(t_i), \quad (3)$$

where $s_{i,m}$ and $w_{i,m}$ represent, respectively, the time-varying parts of the amplitude and phase at time t_i , with i representing a discrete time index. In Equation (1), q_0 represents the mean latitudinal position of the AR configuration at time t . An optimization scheme is then employed to constrain the number of parameters used to represent the toroid belt configuration. The TRR algorithm, introduced in Branch et al. (1999), is a nonlinear optimization algorithm that consists of replacing a function over a high-dimensional functional space by a simpler function that reasonably represents the objective function in a region of the parameter space called the “trust region;” then the variance of the approximate function is iteratively minimized over the trust region until a local minimum is reached. Once a local minimum is reached the algorithm expands the trust region over which it searches for a minimum. In our study, the TRR algorithm converges successfully for longitudinal modes up to $m = 10$ or so, which is more than sufficient for deriving the toroid patterns of our interest, given that we do not see more than 10 latitude–longitude locations where ARs appear. We note that the sequence of times at which the synoptic maps are available is discrete, one for each Carrington rotation (CR),

representing an asynchronous snapshot of the magnetic field configuration of the Sun as observed from the central meridian. Consequently, the time at which significant flare activity takes place will not necessarily agree with the time at which the AR passes through the central meridian. In the meantime, the AR may slightly move in latitude. Therefore, it is important to consider not only the CR at which the flare activity took place, but also previous and following CRs.

2.2. Topological Measures of AR Complexity

Magnetic helicity has been extensively used in plasma physics, and particularly in the context of solar physics. It is a conserved quantity in ideal MHD, and it is generally well preserved even if diffusive effects are present, with slow dissipation rates (Biskamp 2003). A version of the magnetic helicity that is particularly useful for solar magnetic fields is the relative helicity, the helicity calculated relative to a basic state consisting of a potential magnetic field. This version of the magnetic helicity can be computed solely from photospheric fluxes. Early examples of the computation of magnetic helicity budgets in ARs can be found in Chae (2001), Chae et al. (2004), and Kusano et al. (2002, 2004), including the suggestion of possible relationships with flare activity (Moon et al. 2002).

Several studies point to the relative importance of current-carrying helicity for flaring activity. The idea is simple, since potential magnetic fields do not dissipate energy, the more nonpotential a magnetic field configuration is, the more available energy there is to be dissipated in the form of flares. Pariat et al. (2017) proposed, based on numerical simulations, that the ratio between the current-carrying helicity and total relative helicity should be a good indicator of the occurrence of intense flares. The idea of measuring the relative importance of the current-carrying helicity has been applied to the study of observations of ARs that resulted from large flares (James et al. 2018; Moraitis et al. 2019; Green et al. 2022), confirming that a higher degree of current-carrying helicity precedes large flares. A recent study (Liu et al. 2023) performed an extensive study, comprising 21 X-class flares that occurred during SC-24, showing important changes in the free magnetic energy and helicity in the corona, as well as their photospheric fluxes.

More recently, a quantity related to magnetic helicity, called magnetic winding, was introduced in the study of solar magnetic fields (Prior & MacTaggart 2020; MacTaggart & Prior 2021; MacTaggart et al. 2021; Raphaldini et al. 2022). Magnetic winding is related to a well-known topological quantity called the linking number (Arnold & Khesin 2008), and can be seen as a measure of entanglement between field lines. Similar to studies showing that a high contribution of current-carrying helicity is indicative of large flare activity, Raphaldini et al. (2022) showed that magnetic field configurations dominated by current-carrying magnetic winding can also be an indicator of strong flare activity.

In the present study we use magnetic helicity and winding as measures of the complexity of the magnetic field configurations in ARs in CRs presenting strong flares. More specifically, we will study the two ARs that produced the strongest flares during SC-24: AR 12673, which produced the two largest flares of that cycle (one X-9 and one X-8 flare), and AR 11263, which produced the third largest flare of that cycle (an X-6 flare). Here we briefly describe the techniques used to compute the

magnetic helicity and winding; further details can be found in Raphaldini et al. (2022).

2.3. Magnetic Helicity

We start from the definition of relative helicity (Berger & Field 1984) on a bounded volume V with a smooth boundary ∂V :

$$\mathcal{H}_R = \int_V (\mathbf{A} + \mathbf{A}_p) \cdot (\mathbf{B} - \mathbf{B}_p) d^3x. \quad (4)$$

Here \mathbf{B}_p is a reference potential field with a normal component at the surface ∂V coinciding with that of \mathbf{B} , $\mathbf{B} \cdot \mathbf{n} = \mathbf{B}_p \cdot \mathbf{n}$, where \mathbf{n} is the unit vector pointing outward at the surface ∂V . Here we place the surface boundary ∂V at the photosphere, while the volume V is located at the solar atmosphere. \mathbf{A} and \mathbf{A}_p are respective vector potentials (i.e., $\nabla \times \mathbf{A} = \mathbf{B}$ and $\nabla \times \mathbf{A}_p = \mathbf{B}_p$) which are defined up to an irrotational gauge that does not change the value of the integral in Equation (4). The calculation of Equation (4) requires knowledge of the magnetic field in the whole volume ∂V ; in the study of magnetic fields in ARs, this would imply knowledge of the magnetic field in the chromosphere. At this point an assumption has to be made: one alternative is to reconstruct \mathbf{B} from knowledge of its value on the surface ∂V ; another common procedure is to assume that \mathbf{B} is a force-free field, and then reconstruct it from the magnetic field components of ∂V (Thalmann et al. 2011, 2012). An alternative approach is to calculate helicity fluxes through the photosphere. By integrating the fluxes in time one can obtain the accumulated helicity throughout the passage of the AR on the disk (Romano et al. 2014; MacTaggart et al. 2021; Raphaldini et al. 2022). Here, we will follow the second approach. The helicity flux through the surface ∂V is computed as:

$$\begin{aligned} \frac{dH}{dt} &= \int_{\partial V} \frac{d\mathcal{H}(\mathbf{x})}{dt} d^2x \\ &= -\frac{1}{2\pi} \int_{\partial V} \int_{\partial V} B_z(\mathbf{x}) B_z(\mathbf{y}) \frac{(\mathbf{u}(\mathbf{x}) - \mathbf{u}(\mathbf{y})) \times (\mathbf{x} - \mathbf{y})}{|\mathbf{x} - \mathbf{y}|^2} \\ &\quad \times d^2y d^2x. \end{aligned} \quad (5)$$

Here $\mathbf{u}(\mathbf{x})$ is the velocity of the foot-point associated with the magnetic field line at point \mathbf{x} in the photospheric plane. $\mathcal{H}(\mathbf{x})$ is the so-called field-line helicity, which corresponds to the helicity density at point \mathbf{x} .

Consequently the accumulated helicity between times 0 and T is computed by integrating Equation (5) in time:

$$\begin{aligned} H &= -\frac{1}{2\pi} \int_0^T \int_{\partial V} \int_{\partial V} B_z(\mathbf{x}) B_z(\mathbf{y}) \\ &\quad \times \frac{(\mathbf{u}(\mathbf{x}) - \mathbf{u}(\mathbf{y})) \times (\mathbf{x} - \mathbf{y})}{|\mathbf{x} - \mathbf{y}|^2} d^2y d^2x. \end{aligned} \quad (6)$$

Details on the potential/current-carrying decompositions of the magnetic helicity are found in the Appendix, also see Raphaldini et al. (2022) for further details.

2.4. Magnetic Winding

Similarly, the magnetic winding can be computed via a renormalization of the magnetic field to a unit value:

$$f(x) = \begin{cases} I(\mathbf{x}) = 1 & \text{if } B_z(\mathbf{x}) > 0, \\ I(\mathbf{x}) = 0 & \text{if } B_z(\mathbf{x}) = 0, \\ I(\mathbf{x}) = -1 & \text{if } B_z(\mathbf{x}) < 0, \end{cases} \quad (7)$$

then the magnetic winding flux is defined as:

$$\frac{dL}{dt} = -\frac{1}{2\pi} \int_{\partial V} \int_{\partial V} I(\mathbf{x})I(\mathbf{y}) \times \frac{(\mathbf{u}(\mathbf{x}) - \mathbf{u}(\mathbf{y})) \times (\mathbf{x} - \mathbf{y})}{|\mathbf{x} - \mathbf{y}|^2} d^2y d^2x, \quad (8)$$

and the accumulated magnetic winding in the time interval 0 and T :

$$L = -\frac{1}{2\pi} \int_0^T \int_{\partial V} \int_{\partial V} I(\mathbf{x})I(\mathbf{y}) \times \frac{(\mathbf{u}(\mathbf{x}) - \mathbf{u}(\mathbf{y})) \times (\mathbf{x} - \mathbf{y})}{|\mathbf{x} - \mathbf{y}|^2} d^2y d^2x dt. \quad (9)$$

The respective components of the magnetic winding, namely its potential and current-carrying components, are defined in a completely analogous way to the definitions of helicity decompositions and so are omitted here; for further details see Raphaldini et al. (2022). The winding can be seen as a renormalization of the magnetic helicity, by replacing the magnetic field by a field with the exact same orientation, but unit intensity. This can emphasize certain regions of the AR domain with complex structures, but weak radial field, such as polarity inversion lines (MacTaggart et al. 2021; Raphaldini et al. 2022).

2.5. Measures of the Current-carrying and Potential Components

As previously discussed, there is a substantial amount of literature pointing out the role of the emergence of current-carrying-dominated structures before substantial flare activity (Pariat et al. 2017; Green et al. 2022; Raphaldini et al. 2022). Potential magnetic fields cannot dissipate energy through Ohmic processes, but the emergence of current-carrying structures can lead to substantial release of energy in the form of flares.

Raphaldini et al. (2022) introduced a measure of the imbalance between the current-carrying and potential components of magnetic helicity and magnetic winding, named δ measures. First, for the magnetic helicity, this quantity measures at each point of domain \mathbf{x} the difference between the contributions of the current-carrying component of the helicity density $\mathcal{H}_c(\mathbf{x})$ and the potential component of the helicity $\mathcal{H}_p(\mathbf{x})$. We define this instantaneous imbalance as:

$$\delta H' = \int_p (|\mathcal{H}_c(\mathbf{x})| - |\mathcal{H}_p(\mathbf{x})|) d^2x. \quad (10)$$

Analogously the δ measure is defined for the winding as:

$$\delta L' = \int_p (|\mathcal{L}_c(\mathbf{x})| - |\mathcal{L}_p(\mathbf{x})|) d^2x. \quad (11)$$

These quantities are usually very noisy; in the analysis performed in the results section we utilize a smoothed version of these quantities over a time window of 10 hr.

2.6. Helicity and Winding Computations

Here, the computed quantities associated with the magnetic helicity and magnetic winding are performed using the ARTop code⁶ (Alielden et al. 2023). This code computes helicity and winding quantities using the Space-Weather HMI AR Patches (SHARP) data sets corresponding to 12 minute cadence magnetograms for a given AR. The code then used the Differential Affine Velocity Estimator for Vector Magnetograms (DAVE4VM) method (Schuck 2008) to obtain the velocity fields. DAVE4VM uses sequential vector magnetogram images, and assumes a locally linear (or affine) approximation of the velocity field. The evolution of the velocity field is obtained by fitting the linear (affine) coefficients from the evolution of the magnetic field vectors.

3. Results

3.1. An SC Minimum-phase Storm

AR 12673 is well known for being very flare prolific, producing four X-class flares and 27 M-class flares, including the two largest flares of SC-24 (an X-9.3 and an X-8.2 flares; Sun & Norton 2017). The study of this AR, therefore, constitutes a test bed for understanding the circumstances under which flare-prolific ARs are formed, in terms of both global and local dynamics.

One possible reason for the remarkable flare activity of AR 12673 is that it resulted from an emergence at the same location as an old decaying spot (ARs 12665 and 12670). Additionally, AR 12673 was characterized by a very large magnetic flux emergence rate (Sun & Norton 2017), as well as the strongest magnetic field ever recorded in the solar corona. We will investigate the reasons why AR 12673 resulted in such strong flare activity, by analyzing the global magnetic field morphology during CRs 2193–2195 in Section 3.1.1. In Section 3.1.2 that follows, we analyze the magnetic helicity and magnetic winding contained in AR 12673, with particular emphasis on the role of current-carrying and potential-field decompositions.

3.1.1. Analyses of the Prestorm Features of AR 12673 from Global Toroid Patterns

Global toroid patterns of emerged ARs were previously used to infer certain prestorm features, namely for the Halloween storms of 2003 (Dikpati et al. 2021). Primarily three ARs 10484 and 10488 in the north and AR 10486 in the south created the biggest solar storms of cycle 23, causing 11 X-class flares and 46 M-class flares, the largest being an X-28 flare, during a short span of time from 2003 October 19 to November 5. While AR 10486 was the biggest AR of cycle 23, and was a complex $\beta\gamma\delta$ type, much was learned by analyzing the toroid patterns a few CRs before the Halloween storms of CR 2009. Figures 10 and 11 of Dikpati et al. (2021) show how the sustained dominant $m = 2$ longitudinal mode, which produced longitude regions of closest proximity between the north and south toroids as well as furthest away points respectively, created weakening and strengthening of the magnetic field. The furthest away points at the same longitudes of the north and south toroids can be created from the antisymmetric ‘‘tipping’’ of toroids at their deeper origin, at or near the base of the convection zone or tachocline, due to a global MHD instability

⁶ <https://github.com/DavidMacT/ARTop>

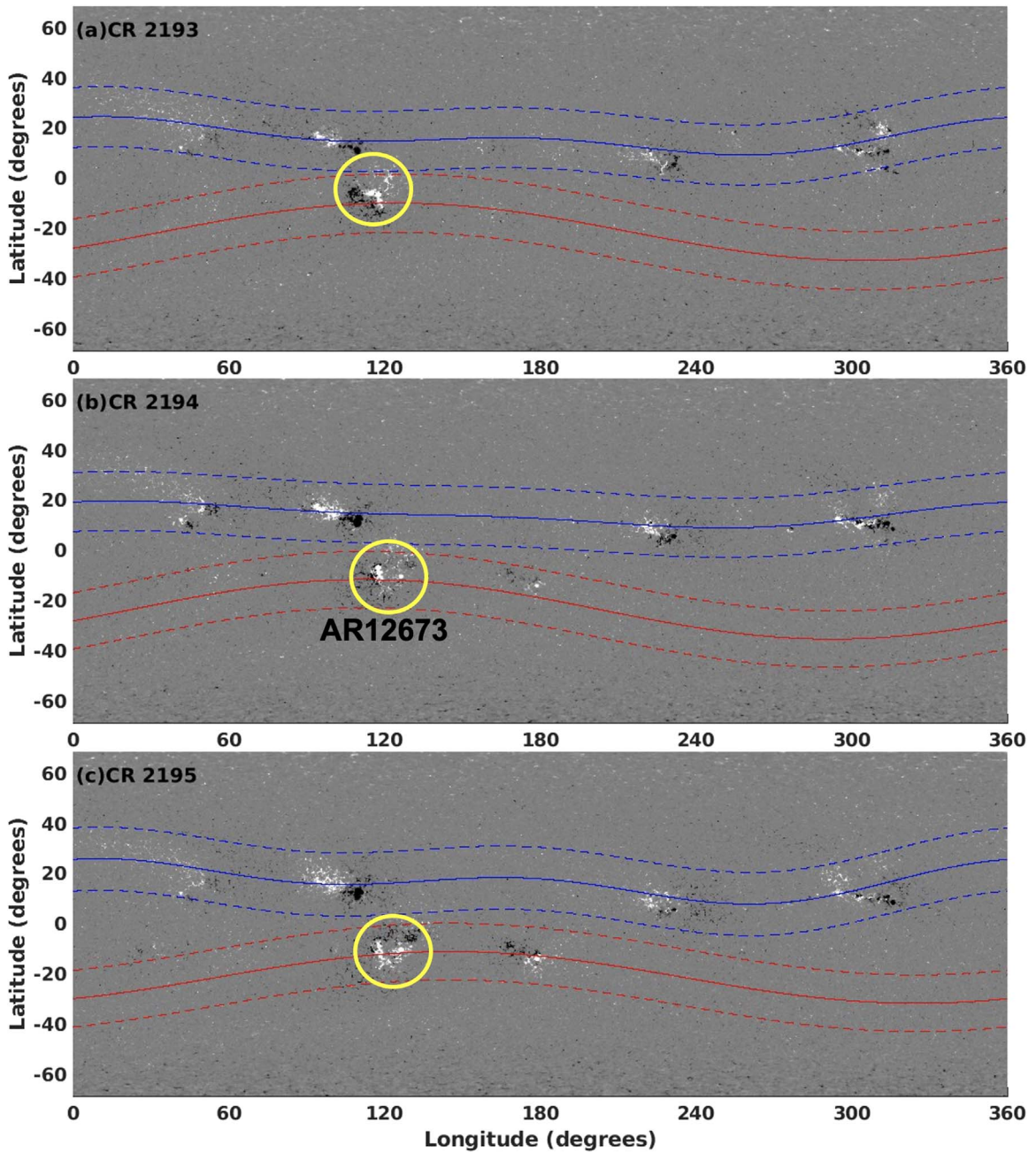


Figure 1. Evolution of the magnetic toroid pattern during CR 2193 (2017 July 20–August 16), CR 2194 (2017 August 16–September 12), and CR 2195 (2017 September 12–October 10), i.e., from one CR before through the storm to one CR after, during which AR 12673, located at 120° longitude in the south (yellow circled region), produced the two biggest flares (X-9.3 and X-8.2) of cycle 24, during the late declining phase near solar minimum.

of spot-producing toroidal magnetic bands. The nonlinear evolution of such instability-produced patterns, being governed by the interaction of Rossby waves with a toroidal band, can be sustained for a few CRs, because Rossby waves drift slowly in longitude. Thus from such nonlinearly evolving toroid patterns the upcoming Halloween storms of 2003 were hindcast and also simulated using a global MHD shallow-water model (see, e.g., Figures 12, 13, and 14 of Dikpati et al. 2021).

To examine whether we can analyze similarly the prestorm features of the biggest storm of cycle 24, which occurred during 2017 September, we derive the toroid patterns for CRs 2193–2195, namely from one CR before the occurrence of the storm through one CR after it. Figure 1 displays how the north and south toroids evolved. The three panels of synoptic maps

clearly reveal several interesting features. First, the toroid patterns are dominated by the $m = 1$ mode in longitude, even though several higher longitudinal wavenumbers are included during the optimization procedure. This is not surprising, because during a late declining or solar-minimum phase, only a few ARs may emerge. Mode fitting in such cases should favor the $m = 1$ mode to be the dominant one. We see that there is one strong and two weak ARs in the north and one moderate AR in the south.

Second, we find that the north and south toroids are locally tipped in antiphase about the equator, but unlike the Halloween storm of cycle 23, the biggest flare-producing AR 12673 of cycle 24 is not located in the tipped-away portions of the toroid. Instead it is in close proximity to another AR of the

south toroid. So, following similar logic given for the Halloween storms' occurrence at the same longitude from the tipped-away portions of the north and south toroids, we note that the global dynamical interactions of the north and south toroids would indicate weakening in their field strengths, and hence hindcasting prestorm properties accurately with a lead time of at least one CR before the storm is not possible in this case; perhaps this is true in the case of the majority of solar-minimum-phase storms.

In fact, weakening of the ARs when the north and south toroids are in close proximity at a certain longitude was really the case for AR 12673 initially; it was decaying and became an apparently inactive spot, and then suddenly got converted to the most active complex region after a new emergence occurred at the center of AR 12673, leading to the biggest flare of that cycle. The new emergence at the center of the old, decaying AR, as well as complex interactions among the north and south toroids' ARs at the same longitude, produced a huge buildup of magnetic helicity. Thus, local dynamics must have played a crucial role a few hours before the trigger of the storm, despite the global dynamics not anticipating a big storm the CR before. In this case, the global toroid patterns derived from the surface distribution of ARs may not be the best indicator of the dynamics of the spot-producing toroidal fields at the bottom, because only very few flux emergences occur then. The 2017 storm is an unusual storm, which has been difficult to understand, simulate, and predict.

Local dynamics themselves lead to only a short lead time of a few to several hours; nevertheless we need to include knowledge gained from local dynamics in prestorm predictive feature analysis for all storms, but particularly for solar-minimum storms. When we examine the buildup of helicity and winding, which exceeds a certain high value to trigger the flares, we point out an important feature derived from the global dynamics for this specific storm during the solar-minimum phase. In particular, how was there a new emergence at the center of the old, decaying spot, which eventually became the most active spot of that cycle? As conjectured and demonstrated by Dikpati & McIntosh (2020), "imprints" of flux emergence correlate with the latitude–longitude location of tachocline bulges, which push up the toroidal field at that latitude–longitude location into the convection zone for their eventual appearance at the surface (see, e.g., Figure 12 in Dikpati & McIntosh 2020). Such bulges, if sustained for several CRs, depending on the global nonlinear dynamical interactions among the differential rotation, toroidal fields, and Rossby waves, can lead to multiple emergences at the same latitude–longitude. This is what happened for the new emergence at the center of the old decaying AR 12673. To understand how that new emergence led to complex interactions with the old inactive AR to make it the most active one of cycle 24 we consider the role of local dynamics in the next subsection.

3.1.2. Analyses of Prestorm Features of AR 12673 from Local Dynamics

Several studies analyzed the topology of the magnetic fields of AR 12673 in terms of its magnetic helicity. Vemareddy (2019) showed a rapid input of helicity before the occurrence of the major flares, while Moraitis et al. (2019) highlighted the role of the current-carrying component of the helicity. More recently, Raphaldini et al. (2022), computed the magnetic

winding, a direct measure of the topology of the magnetic field configuration, to show that, compared with other ARs, the complexity of the magnetic field of this region is much more dominated by current-carrying structures.

Figure 2 shows the evolution of the magnetic field and helicity densities throughout the AR 12673 lifetime. Up to time $t = 100$ hr after the appearance of AR 12673 on the disk both the magnetic fields (see Figures 2(a) and (c)) and the helicity (see Figures 2(b) and (d)) are dominated by a single spot, reminiscent of ARs 12665 and 12670 during previous CRs. It is also notable that at time $t = 100$ hr the helicity structure is weaker than it was at $t = 10$ hr, suggesting a decay or diffusion of helicity throughout this time span; on the other hand the magnetic field structure displays a magnetic field that remains coherent. At this point new magnetic field structures start to emerge around the old spot, which remains relatively unperturbed by the new emergence. At $t = 150$ hr (Figures 2(g) and (h)) increased complexity in the pattern of magnetic fields and magnetic helicity is present, with the imprint of the old spot still present. At $t = 200$ hr, close to the sequence of two intense X-class flares, including the X-9 flare, we see a remarkably complex magnetic field structure, characteristic of a δ spot, where the imprint of the old spot can still be identified. This interaction between different emergences at the same location clearly played a role in the complexity of the magnetic fields in AR 12673, raising some important questions: How do the large-scale magnetic fields and flows at the depth where the emergences originate favor the sequential rise of magnetic fields through the convection zone? What are the large-scale patterns that favor these sequential emergences? How does the old decaying spot remain so stable despite of the strong perturbations resulting from the secondary emergence of AR 12673?

The accumulated helicity and winding time series are illustrated in Figure 3 where it is shown that very little magnetic helicity and winding are accumulated while the old spot is the dominant structure, until about 120 hr after emergence. As soon as the second emergence takes place, a steady accumulation of helicity and winding with flare activity is initiated a few hours after. The flare activity is initially comprised of C-class flares, followed by a sequence of M-class flares at around 170 hr. As the helicity and winding increase, accompanied by several M-class flares, two sequential X-class flares appear, separated by 3 hr, at around 220 hr, including the X-9.3 flare. The X-class flares are accompanied by a small inflection in both curves. About 20 hr after the X-9.3 flare, another X-class flare was produced, this time an X-1.3 flare. Two days later another X-class flare, an X-8.3 flare, was produced, which is not presented here since it took place when the AR was near the border of the disk.

Next, we analyze the imbalance between the current-carrying and potential parts of the helicity and winding, also known as the δ quantities defined in Equations (10) and (11). Since these signals are very noisy we present a smoothed version of $\delta H'$ and $\delta L'$ over a 10 hr window. We present the evolution of the δ quantities for AR 12673 in Figure 4. As expected, very little imbalance is observed in AR 12673 while it has an α -type single-spot structure. Once the second emergence takes place an imbalance develops in both the magnetic helicity and winding. We notice that the first response is seen in the winding imbalance, with negative values, indicating that in the early stages of the secondary emergence the magnetic field

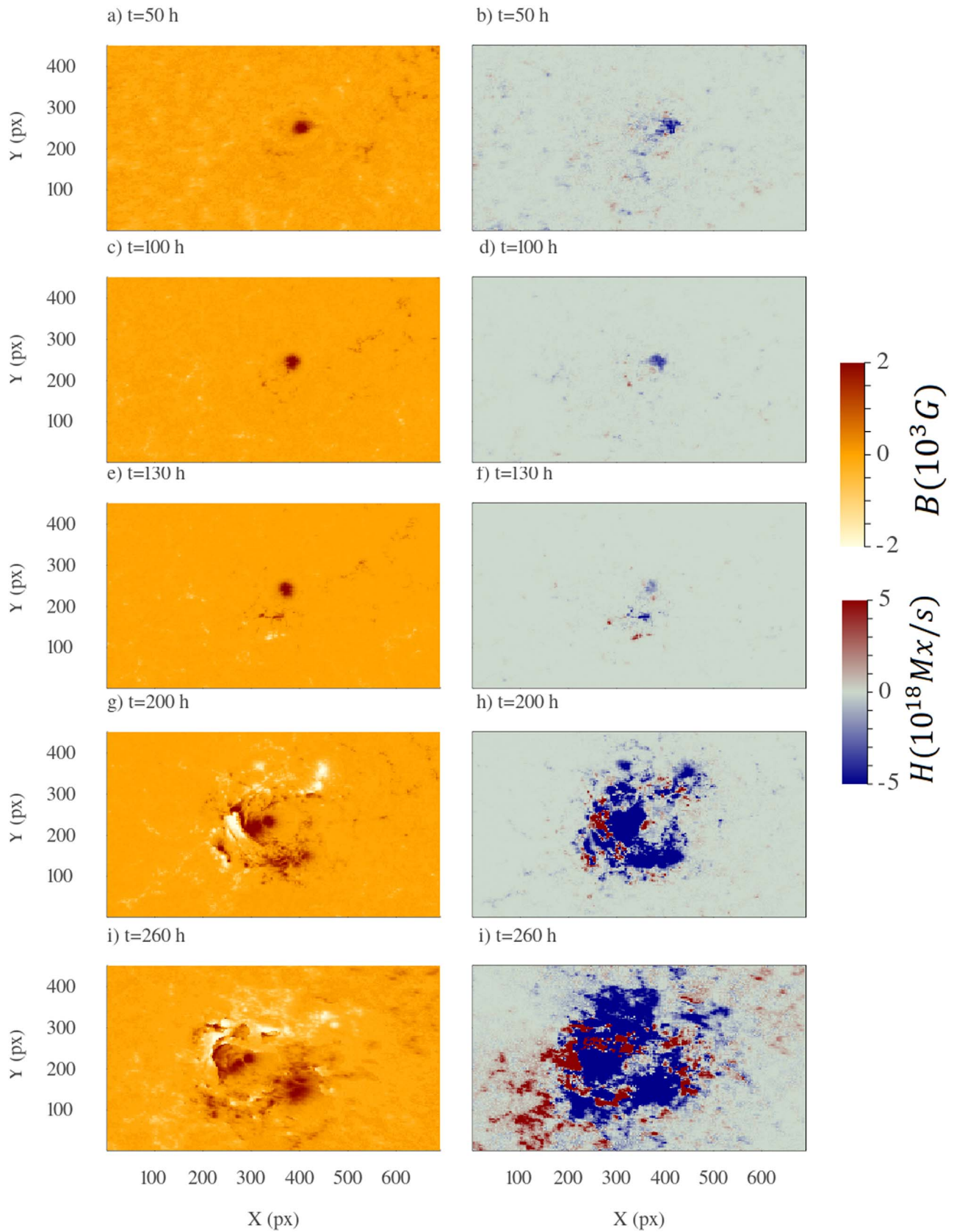


Figure 2. Evolution of the magnetic fields (left) and helicity flux (right) for AR 12673. An animation of the continuum intensity and magnetogram associated with this figure is available. The animation runs from 2017 August 29 at 19:00:00 and ends on 2017 September 9 at 18:12:00, corresponding to the limb-to-limb evolution of this AR. The real-time duration of the animation is 11 s. The dimensions of the pixels are defined in Bobra et al. (2014). The original video file is available at DOI:10.5281/zenodo.8305952.

(An animation of this figure is available.)

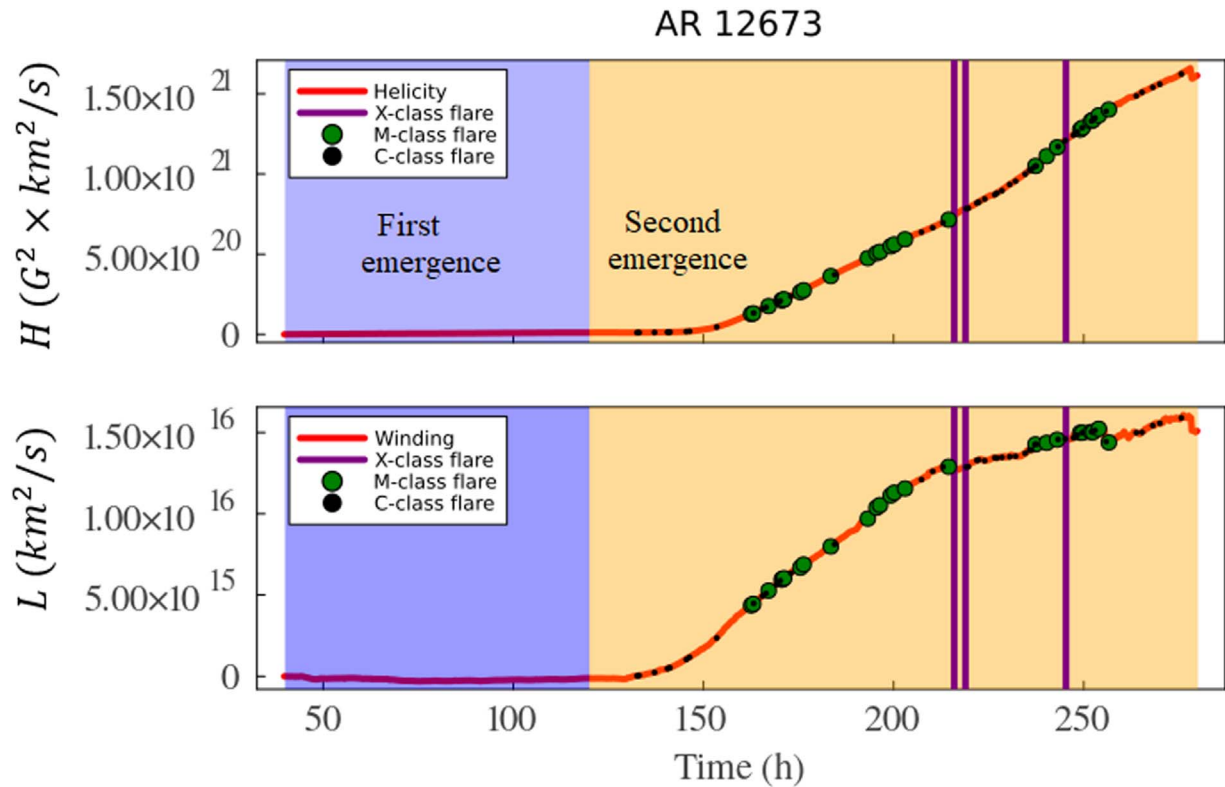


Figure 3. Accumulation of magnetic helicity (top) and magnetic winding (bottom) for AR 12673. Purple and beige backgrounds indicate first and second major emergences, respectively. Here, the start time is 2017 August 28, 09:00.

structures have low intensity and are primarily potential. Once the winding imbalance starts becoming positive an imbalance in the helicity also starts developing, with both now indicating current-carrying dominance, and the increase in both indicates that complex morphologies are present in these regions with strong magnetic fields. The difference between both curves can be understood from the fact that, while the helicity is weighted by the magnetic field strength, the magnetic winding is not. The helicity imbalance in particular shows a clear pattern of increasing before X-flare activity, followed by a decrease, probably due to dissipative relaxation due to the reconnection of magnetic field lines.

3.2. An SC Peak-phase Storm

Having derived the pre-solar-storm features of an AR that resulted in strong flare activity during the solar-minimum phase, we now compare them with the features of a flare-producing AR, AR 11263, during the peak phase of cycle 24.

AR 11263 appeared on the east limb of the visible disk on 2011 July 28, during the late rising phase of cycle 24. It is to be noted that cycle 24 exhibited widely separated double peaks—the first peak occurred in 2011 in the northern hemisphere, while the second peak was in 2014 in the south (Pesnell 2016). AR 11263 occurred near the first peak in the then dominant northern hemisphere. It appeared on the disk already with a $\beta\gamma\delta$ configuration, producing a C-class flare within a day after its appearance. It kept a moderate level of activity until the AR evolved a more complex structure, and a consequent increase in the level of activity around August 3, resulting in an M-class flare. On August 8 a second emergence took place, further increasing the level of complexity of the AR, leading to a sharp increase in the level of activity, resulting in two M-class flares

and one X-class flare (X-6.9), the third largest flare of SC-24. After that, the level of activity decreased, with the AR presenting a few C-class flares before it moved to the limb.

What can we analyze with one CR lead time from the global toroid pattern? In the following two sections, Sections 3.2.1 and 3.2.2, respectively, we present the results from the global magnetic field configurations during CRs 2112–2114 and the magnetic helicity and winding input of AR 11263, as well as current-carrying and potential decompositions, several hours before the X-flare.

3.2.1. Analyses of the Prestorm Features of AR 11263 from Global Toroid Patterns

The three panels of Figure 5 display the evolution of toroid patterns, derived from the surface distribution of ARs, during CRs 2112–2114. AR 11263 is located in the yellow circled region, at a longitude of 300° in the north. In the same toroid we mark another nonflaring AR, AR 11266, by a pink circle, located at about 245° longitude, to compare the prestorm features of flaring and nonflaring ARs.

Several features are immediately revealed from these three panels. First, both the north and south toroids show sustained multimode patterns, with the north toroid dominated by the $m = 1$ longitudinal mode and the south by the $m = 1, 2,$ and 3 modes. The northern hemisphere magnetic activity being much stronger than in the south during 2011 is expected since the $m = 1$ mode is a characteristic of the tipping of a toroidal ring that behaves rigidly like a “steel ring” (Cally et al. 2003). Cally et al. (2003) showed that a toroidal ring tips with an $m = 1$ pattern when the magnetic field is strong enough, typically more than 30 kG, whereas weak rings with field strengths smaller than 30 kG deform, revealing a pattern dominated by $m > 1$ modes.

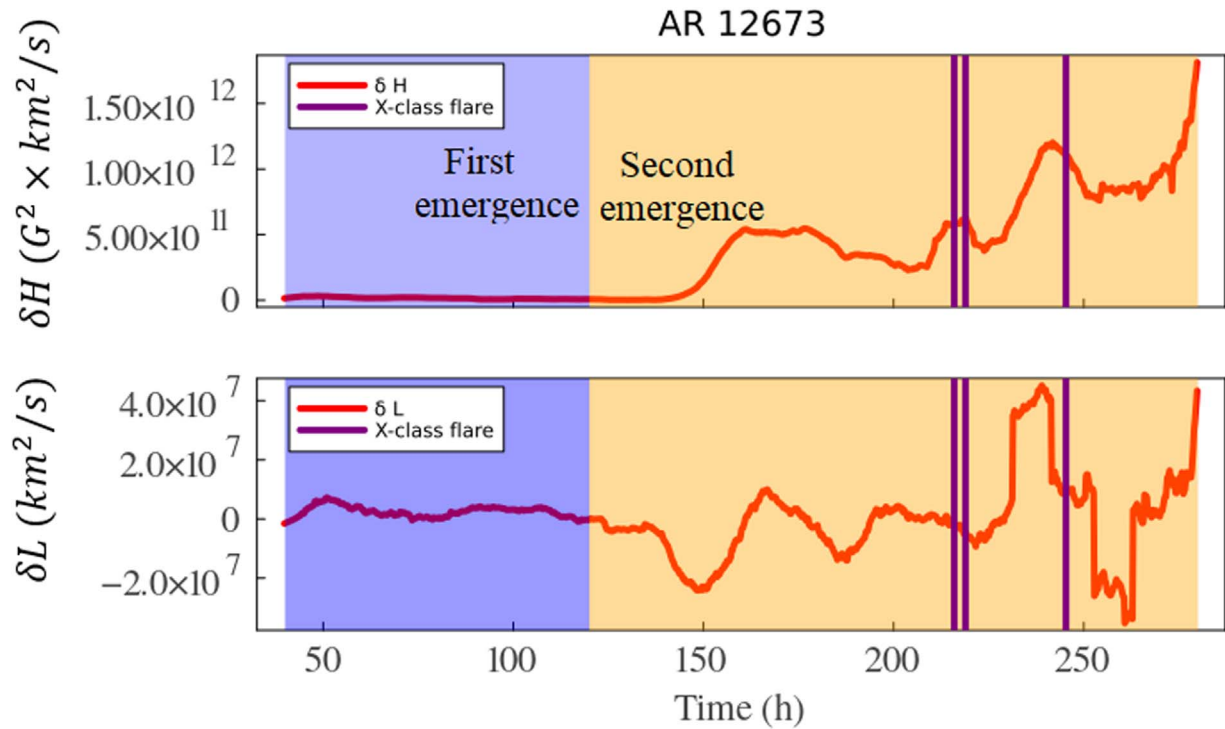


Figure 4. Evolution of the magnetic helicity imbalance (top) and magnetic winding imbalance (bottom) for AR 12673. Negative values indicate the injection of potential-dominated magnetic structure and positive values indicate current-carrying-dominated magnetic field structure. Purple and beige backgrounds indicate first and second major emergences, respectively.

Thus a dominant $m = 1$ pattern in the north during the 2011 storm caused by AR 11263 reveals the stronger toroidal band in the north than in the south. Second, AR 11263 appears in the tipped-away portions of the north and south toroids, whereas AR 11266 appears in a latitude–longitude location where the north and south toroids are closer to each other, thus allowing strengthening of AR 11263 and weakening of AR 11266 due to interactions between oppositely directed toroids. The global patterns here are much closer to those during the Halloween storms of cycle 23, except that cycle 24 was altogether much weaker than cycle 23. The prestorm features from CR 2112 indicate the possibility of upcoming big storms from AR 11263 within one or two CRs, and perhaps much less possibility of storms occurring from AR 11266.

A comparison of Figure 5 with Figure 1 clearly reveals relatively much more sustained patterns in the evolution of toroid during the peak phase with respect to that during the minimum phase of the cycle. This is related to the deeper origin of these warped toroid patterns, which are most likely produced by the interaction of Rossby waves with the dynamo-generated toroidal magnetic fields. Those Rossby waves were found to have variations in their drift speed in longitude as function of latitude. Figure 7 of Dikpati et al. (2018a) shows that the phase speed is close to zero when the toroidal band is around 20° latitude, which is the case here for the peak-phase toroid patterns during CRs 2112–2114. The more sustained these patterns are the more flare prone the big and complex ARs are from the tipped-away portions of the toroids.

While the peak-phase storms are more predictable, with a significant lead time, from the analysis of global toroid patterns, the obvious question is: what additional prestorm features can we find from the local dynamics several hours ahead of the storm?

3.2.2. Analyzing the Prestorm Features of AR 11263 from Local Dynamics

The evolution of the magnetic field morphology in AR 11263 is described in Figure 6. There we see that the AR appeared on the disk, first as a simple β -type spot, until at around $t = 200$ hr a second emergence interacted with the β configuration resulting in a complex magnetic field configuration, a $\beta\gamma\delta$ -type structure. The evolution of the magnetic field and helicity densities is depicted in Figure 6.

The analysis of the accumulated magnetic helicity and winding for this AR is presented in Figure 7. Initially AR 11263 showed negative helicity accumulation which was reversed by added positive helicity starting at around 85 hr, which persisted until roughly $t = 200$ hr, followed by a small decrease in the total winding. As soon as the second emergence took place, a slow but steady increase in the helicity took place until the time of the X-6.9 flare. In terms of the accumulation of magnetic winding, the overall trend was similar, except that the winding presented an almost steady increase from $t = 100$ hr until the time of the X-flare at around $t = 300$ hr. A sudden relative rapid increase in the winding curve was observed following the second emergence at around $t = 250$ hr, which became more evident about 10 hr before the flare happened.

The results from the magnetic helicity and magnetic winding decompositions into potential and current-carrying fields is presented in Figure 8. The helicity and winding imbalances (or δ -measure) for the magnetic helicity imply an overall dominance of potential structures, followed in time by a stable input of current-carrying-dominated structures from $t = 85$ hr until time $t = 180$ hr, and after that, a decrease in $\delta H'$ that indicates a balance between potential and current-carrying helicity between $t = 200$ and $t = 250$ hr. Starting at time $t = 250$ hr, two impulses occur in $\delta H'$, the second-largest and

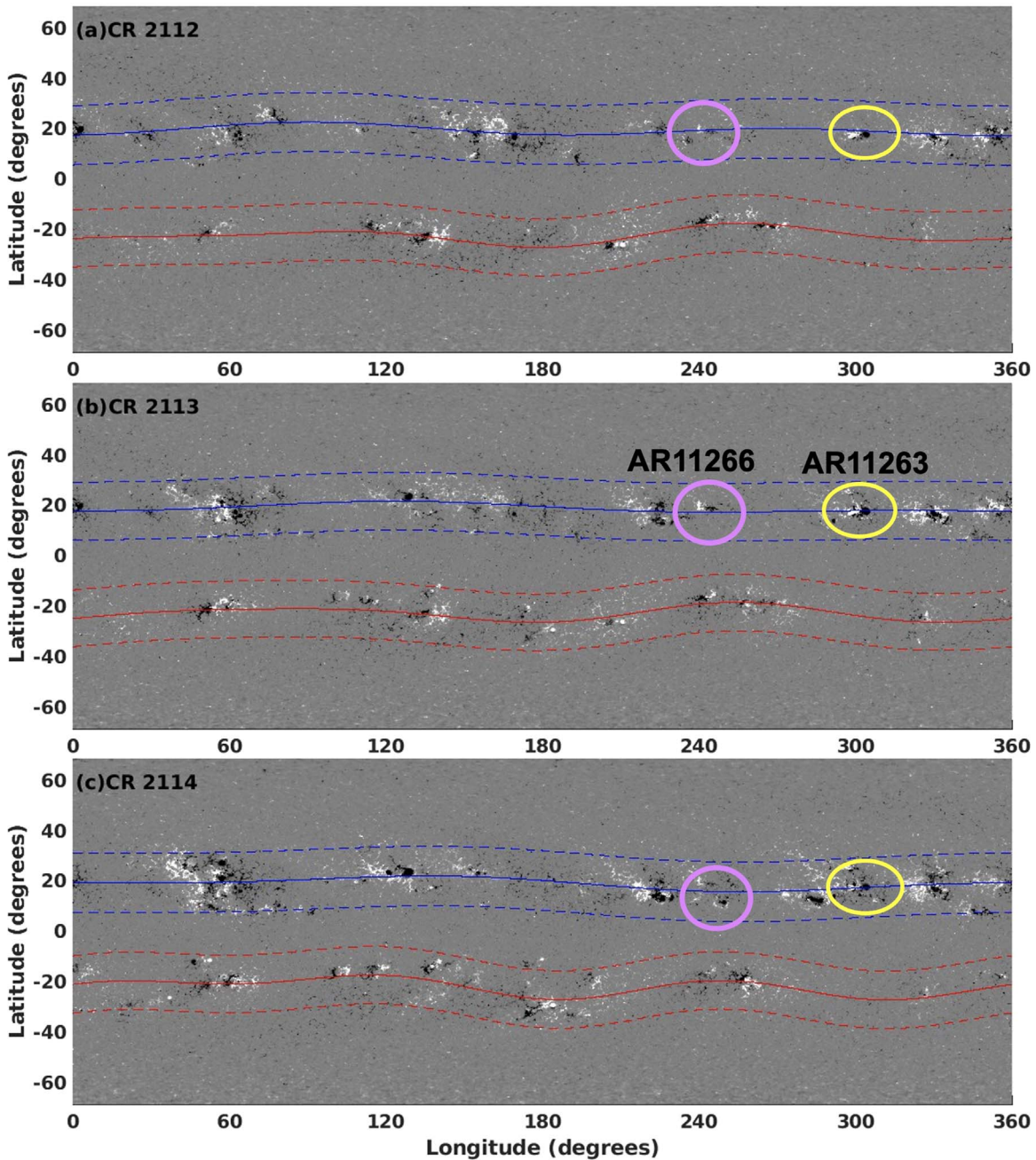


Figure 5. Evolution of the magnetic toroid pattern during CR 2112 (2011 July 3–July 30), CR 2113 (2011 July 30–August 26), and CR 2114 (2011 August 26–September 22), i.e., from one CR before through the storm to one CR after, during which AR 11263, located at 300° longitude in the north (yellow circled region), produce the second-biggest flare (X-6.9) of cycle 24. Another AR (AR 11266, marked by pink circled region) in the same toroid, located at a longitude of about 55° left of AR 11263, did not flare.

largest ones leading up to the X-class flare. The magnetic winding imbalance, on the other hand, showed a fluctuating behavior with a predominance of potential fields after the second emergence, indicating that in the beginning the secondary emergence was characterized by weak potential fields, similar to what is observed in AR 12673. At around $t = 250$ hr there was a steady increase in this quantity, followed by a sharp increase just before the flare. Again, as in the case of AR 12673, the magnetic helicity and winding imbalance show a clear tendency of increasing before the major flare, which is more evident for the magnetic helicity, confirming the role of the injection of current-carrying-dominated structures, leading up to the X-class flare events.

3.3. A Peak-phase AR, AR 11266, Triggering no Storm

AR 11266 emerged on the disk on 2011 August 1, just a few days after AR 11263; it was the first AR to emerge on the northern hemisphere following AR 11263. Throughout its transit across the disk it was characterized by a β -type structure with well-defined positive and negative polarities. The ARs started losing coherence at around 180 hr. Figure 9 shows the evolution of the magnetic fields in AR 11266; we can see that the magnetic field morphology in AR 11266 starts losing coherence after about $t = 200$ hr. So, unlike the in the cases of AR 12673 and AR 11263 analyzed in Sections 3.1.2 and 3.2.2, the simple initial configuration remained until it decayed, instead of interacting with a new emergence.

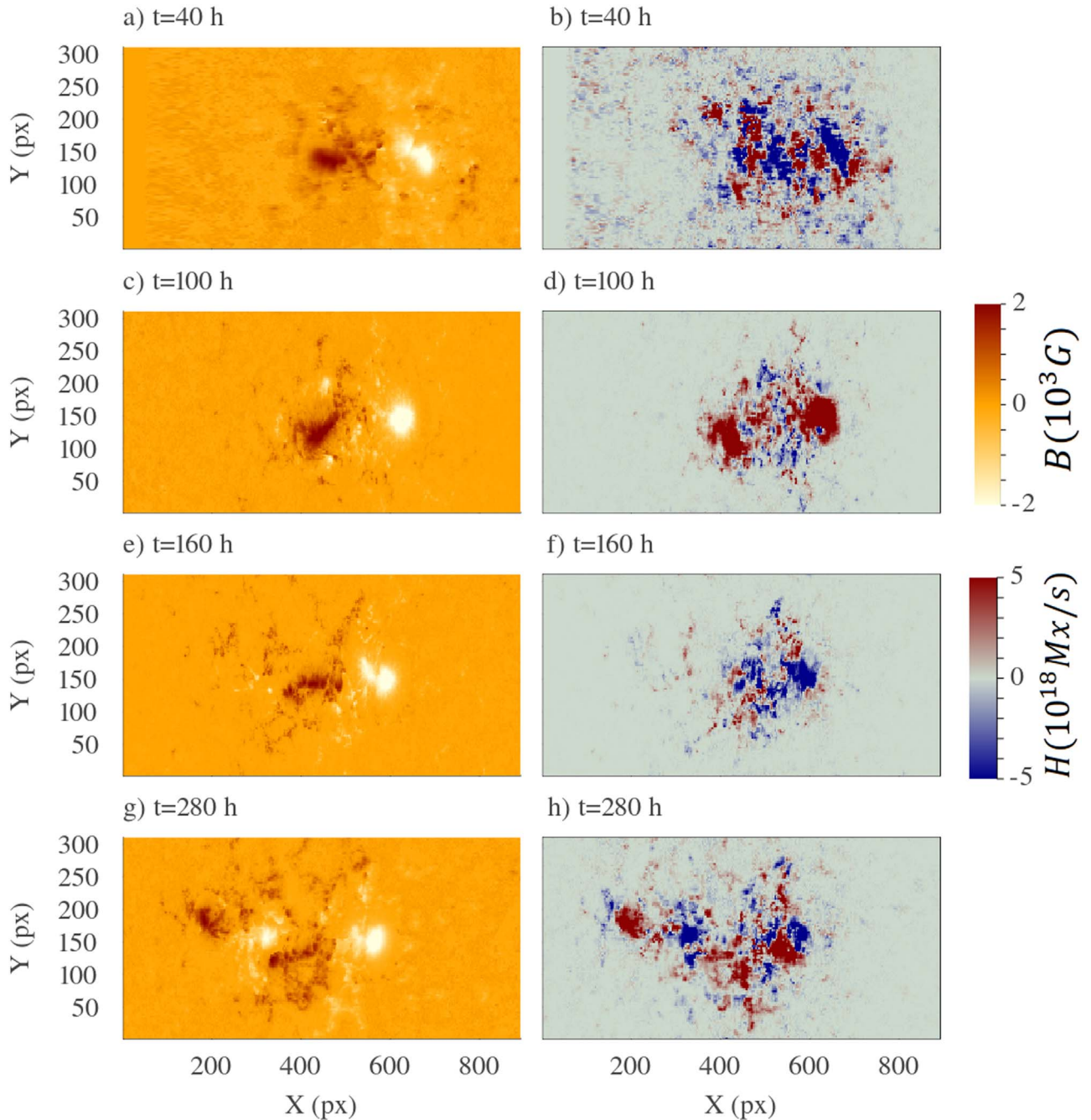


Figure 6. Evolution of the magnetic fields (left) and helicity flux helicity (right) for AR 11263. An animation of the continuum intensity and magnetogram associated with figure is available. The animation runs from 2011 July 28 at 11:12:00 and ends on 2011 August 9 at 22:24:00, corresponding to the limb-to-limb evolution of this AR. The real-time duration of the animation is 12 s. The original video file is available at DOI:[10.5281/zenodo.8305952](https://doi.org/10.5281/zenodo.8305952).

(An animation of this figure is available.)

Figure 10 shows the evolution of the accumulated total magnetic helicity and winding. In terms of the accumulation of magnetic helicity and winding, both quantities show a very similar behavior with a slow increase up to $t = 130$ hr, followed by a rapid impulse until $t = 160$ hr, after which the accumulation of both quantities slowed down. The inspection of $\delta H'$ and $\delta L'$ reveal the nature of the rapid increase in the accumulated helicity and winding around $t = 150$ hr. Both the winding and helicity imbalances, shown in Figure 11, demonstrate a clear dominance of potential structures during this time. Unlike AR 12673 and AR 11263, this AR did not

present any major event of injection of current-carrying-dominated structures, which explains why it did not flare.

4. Summary

Here, we summarize our main findings.

1. Prestorm features were studied both in terms of the global distribution of ARs and individual configurations.
2. Techniques based on the individual AR magnetic field characteristics provide several hours (Leka et al. 2019a; Kusano et al. 2020) of lead time before major X-class

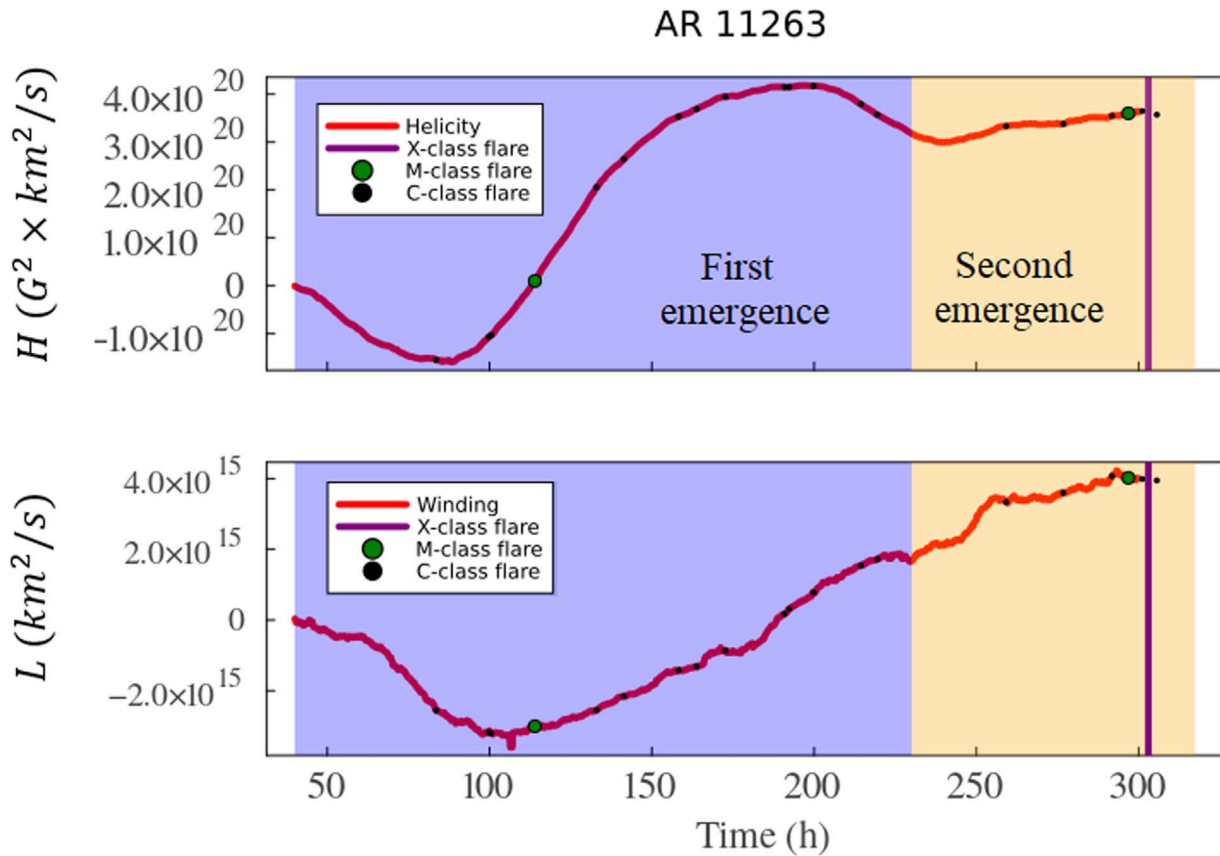


Figure 7. Accumulation of magnetic helicity (top) and magnetic winding (bottom) for AR 11263. Purple and beige backgrounds indicate first and second major emergences, respectively. We note that after the X-class flare the AR approaches the limb, therefore the data become less reliable and are omitted. Here the start time is 2011 July 27, 12:00.

flare events occur, leaving a short time for society to prepare against their hazardous effects. The identification of particular characteristics of the global magnetic field structure can potentially provide one CR of lead time before big storms.

3. The two most flare-prolific ARs of SC-24 were analyzed: AR 12673, which occurred approaching solar minimum, and AR 11263 which occurred near maximum.
4. Two classes of techniques were used to investigate the prestorm conditions: toroid tipping patterns were fitted to the global distribution of ARs, and the individual magnetic field morphologies of ARs were studied using the topological measures of magnetic helicity and winding.
5. AR 12673 emerged in the declining phase of SC-24, in 2017 September, when the solar photosphere was not populated by many ARs. As a result, the toroid fitting procedure presented in Section 4 showed a magnetic field band dominated by the $m = 1$ wavenumber, in such a way that a tipping pattern could not be well determined.
6. The strong flare activity of AR 12673 resulted from the interaction between an old decaying spot and a new emergence, producing a highly complex magnetic field configuration. The local analysis showed that this interaction between an old spot and a new emergence resulted in a highly nonpotential structure leading up to major X-class flares.

7. For AR 11263, the toroid fitting procedure performed in subsection revealed a scenario that is similar to that of the Halloween storm of 2003 (Dikpati et al. 2021). In particular, AR 11263 appeared in a portion of the toroid where the northern and southern hemisphere belts tip away from each other.
8. Like AR 12673, the X-class flare produced by AR 11263 occurred after a new emergence took place at the same location where the β -structure was situated, resulting in a structure dominated by a nonpotential field.
9. AR 11266 was an AR adjacent to AR 11263. AR 11266 appeared as a β -type structure that remained as such until it started diffusing out, toward the latter stages of its passage through the disk. The toroid fitting analysis shows that, unlike AR 11263, it was situated in a longitude where northern and southern hemisphere toroids come close to each other. And, unlike the cases of AR 11263 and AR 12673, the emergence of AR 11266 was dominated by potential structures, which help us understand why it did not produce any flares at all.
10. Comparison of Figures 4, 8, and 11, with 3, 7, and 10 suggests that the magnetic helicity and winding imbalance quantities are a better predictor than the respective raw quantities. This highlights the importance of relative contribution of current-carrying helicity and winding.

Figure 12 and Section 4 summarize the findings in terms of the maximum imbalance found in the helicity and winding

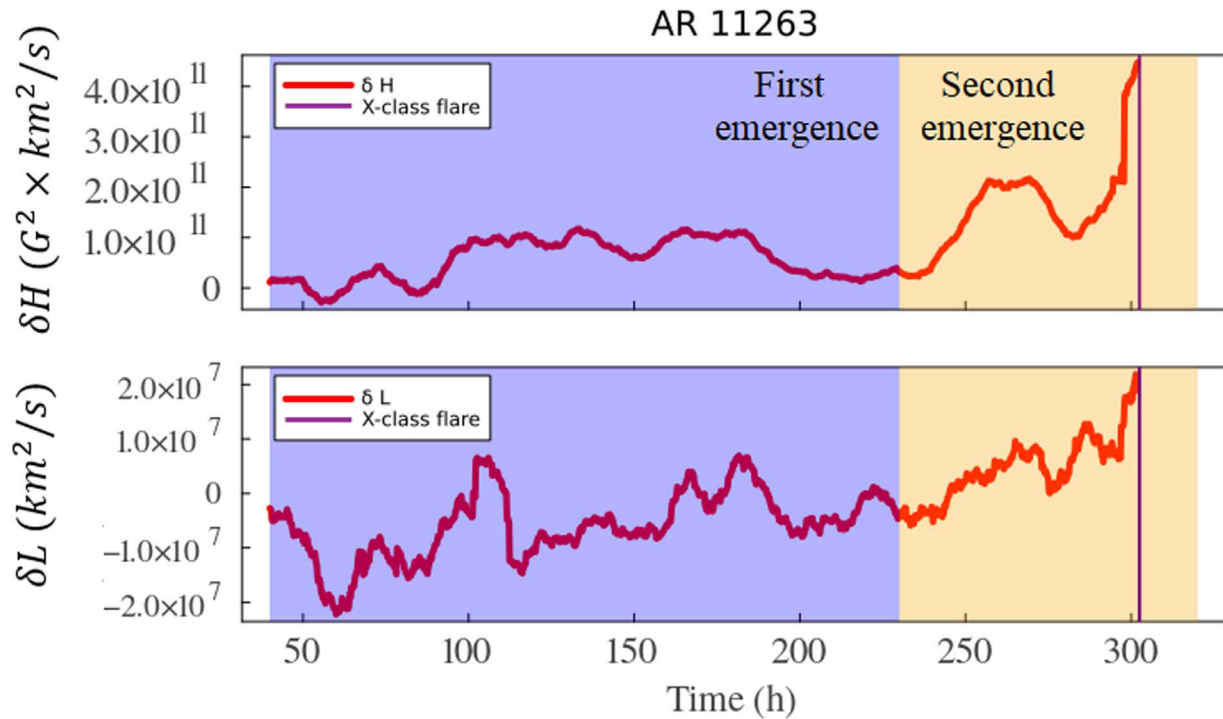


Figure 8. Evolution of the magnetic helicity imbalance (top) and magnetic winding imbalance (bottom) for AR 11263. Negative values indicate the injection of potential-dominated magnetic structure and positive values indicate current-carrying-dominated magnetic field structure. Purple and beige backgrounds indicate first and second major emergences, respectively.

analyses, representing either the main emergence event dominated by potential (negative) values of current-carrying (positive) structures.

AR	H	L	δH	δL
11266	5.1×10^{19}	2.1×10^{15}	-4.6×10^{11}	-1.8×10^7
11263	4.2×10^{20}	4.1×10^{15}	4.4×10^{11}	2.2×10^7
12673	1.8×10^{21}	1.5×10^{17}	1.5×10^{12}	4.3×10^7

5. Concluding Remarks

Forecasting the upcoming enhanced bursts of solar activity well ahead of time no doubt has significant societal value. The majority of energetic flares and CMEs that can adversely impact the technological infrastructure occur during such bursty “seasons” of activity. So far primary emphasis has been given to forecasts of solar energetic phenomena occurring on hours-to-days timescales and the configuration and evolution of individual ARs that are responsible for causing the events. These studies are important, and can have a lead time of a few to several hours to send out an alert. However, often predicting an upcoming solar storm with only hours of lead time may not be enough to protect society from their hazardous impacts.

In a recent study by Dikpati et al. (2021), in the context of analyzing the pre-solar-storm features of the 2003 Halloween storm, which caused multiple X-class flares, including an X-45 flare (Thomson et al. 2004), the latitude–longitude location of ARs in a warped toroid and their evolution were found to play crucial roles in predicting the possibility of big storms. Using an MHD shallow-water model, which allows nonlinear interactions among Rossby waves, spot-producing toroidal fields at the base of the convection zone or tachocline and the differential rotation therein, the occurrence of Halloween

storms from the same longitudes in both hemispheres within an interval of a few days was explained as originating from the tipped-away portions of warped toroids. When the toroidal bands coincide with the bulgings or high-pressure regions of the top surface of the shallow-water model, the flux can be pushed to the convection zone for buoyant rise to the surface. In the case of the Halloween storms of 2003, toroid patterns indicated the “sympathetic emergences” of ARs at the same longitude in both hemispheres, and the toroid patterns evolved very slowly, revealing a sustained tachocline top-surface bulging. In such situations global toroid patterns and their evolutions can be used to forecast the possibility of upcoming big storms.

In the present work, we examined whether we can forecast the biggest storm of cycle 24, namely the 2017 September storm, by studying the evolutionary patterns of the global toroid. By using an optimization technique based on the TRR algorithm, we derived the toroid patterns for three CRs covering the span before and after the storm. We found that the patterns were strongly dominated by $m=1$ mode in longitude. Noting that the 2017 September storm occurred during the minimum phase of cycle 24, we can expect $m=1$ toroid patterns because only a few ARs would emerge at that cycle phase. Even though toroid patterns indicated “sympathetic emergences” in both hemispheres, the northern and southern hemispheres’ ARs were not from the tipped-away portions of the north and south toroids; instead they were in close proximity. Thus they are expected to weaken each other, decreasing the possibility of big storms. However, due to the new emergence at the center of the apparently inactive decaying AR 12673 in the south, that AR became extremely active due to complex interactions among old and new ARs, and caused the biggest storm, including four X-class flares (the

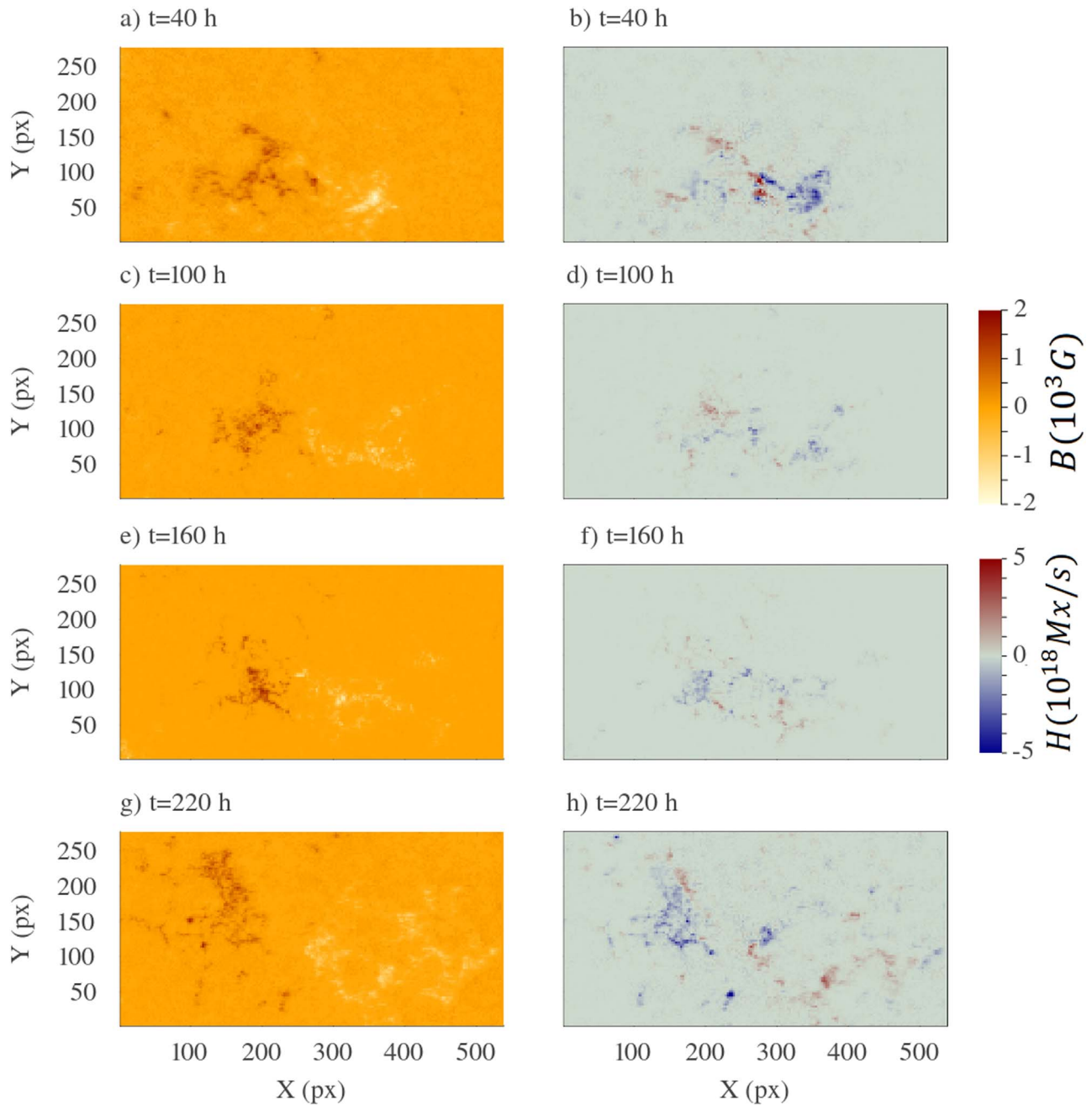


Figure 9. Evolution of the magnetic fields (left) and helicity flux (right) for AR 11266. An animation of the continuum intensity and magnetogram is available. The animation runs from 2011 August 2 at 09:48:00 and ends on 2011 August 13 at 22:00:00, corresponding to the limb-to-limb evolution of this AR. The real-time duration of the animation is 12 s. The original video file is available at DOI:10.5281/zenodo.8305952.

(An animation of this figure is available.)

biggest one being X-9.3, the biggest of cycle 24) and 27 M-class flares.

While global toroid patterns can explain why new emergences occurred at the same longitude, namely due to sustained bulging of the shallow-water tachocline top surface containing a toroidal band, we need additional physics to understand this solar-minimum-phase storm, obtained through analyses of the configuration and evolution of AR 12673 as a function of time. Thus, by analyzing the measures of magnetic field topology and complexity, namely magnetic helicity and magnetic winding, we can understand that the rate of huge buildup of the current-carrying structure in the configuration of

AR 12673 within about 100 hr from the new emergence at the center of decaying AR 12673 was the major cause of the 2017 September solar storm.

In general minimum-phase solar storms are bound to be unusual, due to originating from ARs that do not strictly follow sustained toroid patterns. Hence, unlike the Halloween storms of 2003, the 2017 September storm cannot be speculated with one CR lead time just from the analysis of the global toroid patterns. Additional physics from the local configuration and evolution of the AR responsible for causing the storms were necessary to speculate on this storm, with the lead time reduced to several hours from several days.

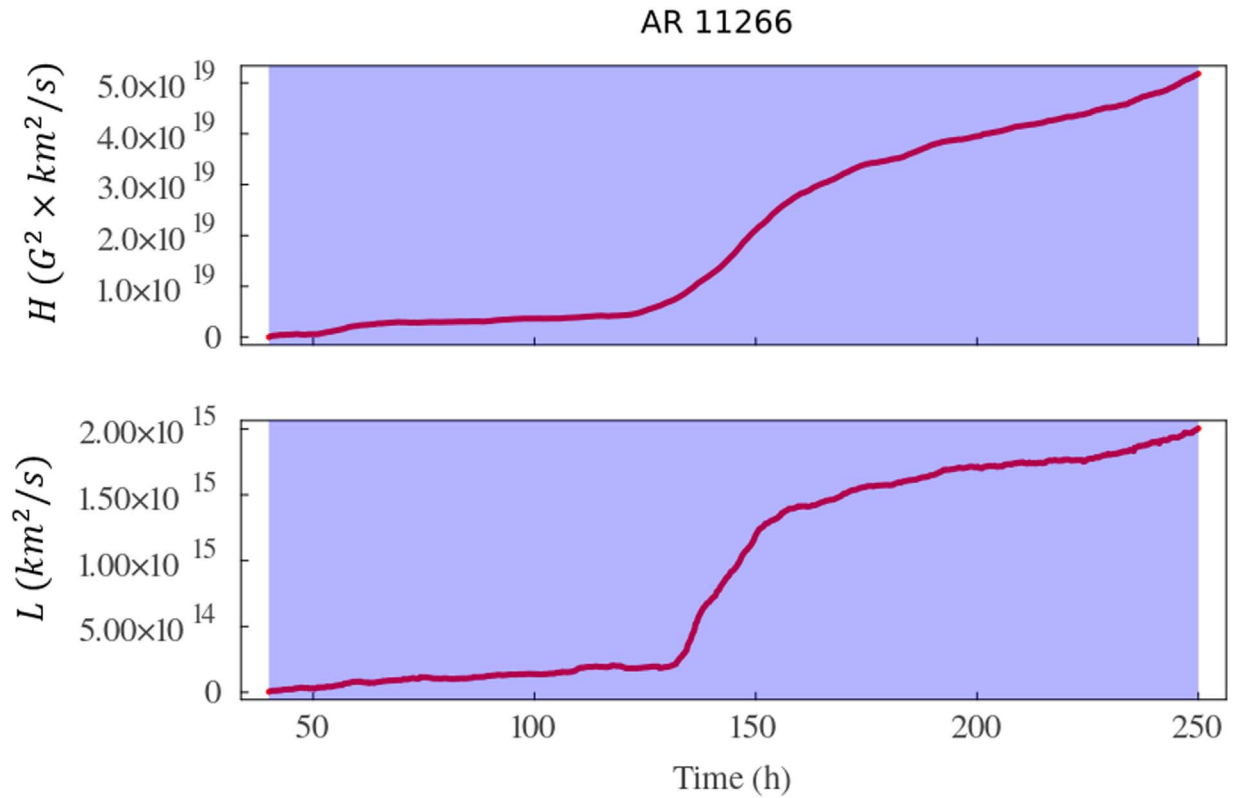


Figure 10. Accumulation of fluxes magnetic helicity (top) and magnetic winding (bottom) for AR 11266. Here, the start time is 2011 August 2, 10:00.

On the other hand, the second-biggest storm of cycle 24 occurred during 2011 August, during the peak phase of that cycle. So, very much like the Halloween storms occurring during the peak phase of cycle 23, we showed that the prestorm features of slowly evolving magnetic toroid patterns could anticipate the 2011 August storm originating from AR 11263; this storm occurred from an AR in the tipped-away portions of the north and south toroids. This forecast is possible because many ARs emerge during the peak phase, and lead to toroid patterns with multiple m -modes. Furthermore, the toroid patterns evolve slowly, because the speed of the magnetically modified Rossby waves is very slow at latitudes of $\sim 15^\circ$ – 20° where the toroids are located during the peak phase of a cycle. Sympathetic emergences can occur too due to sustained bulging.

What can the local dynamics add to the prestorm features for predicting storms in this case? The magnetic helicity and winding analysis for AR 11263 indicated a substantial injection of current-carrying structure, even though they one order of magnitude less than that in AR 12673, which eventually caused the occurrence of the second-biggest flare (of class X-6.9) of cycle 24.

Around the time of AR 11263 the Sun was populated with many sunspots. In order to understand how the latitude–longitude location on the warped toroid can be indicative of the prestorm properties of the AR, we analyzed another AR, AR 11266, which emerged about 45° away in longitude compared to the neighboring AR 11263. Analysis of the toroid patterns indicated that AR 11266 was located in the portion of the toroid which was in close proximity of its opposite hemisphere counterpart, and hence got weakened due to the interaction between them. Obviously big storms are not anticipated from this AR from the global toroid analysis. However, during the

lifetime of this AR complexity may arise from new emergences at the same longitude; hence the study of local dynamics is necessary. The magnetic helicity and winding computation showed that this AR was neither associated with a sympathetic emergence nor a current-carrying structure developed during its lifetime. Thus this AR did not produce a flare, confirming the prestorm conjectures we derived from both the global and local dynamics.

We conclude, from the main findings from the analysis of prestorm properties, that global toroid patterns and their slow evolution during the peak phase can lead to major flare activity from ARs, which emerge in a longitudinal position where northern and southern hemisphere toroids tip away from each other. This gives enough lead time to follow how the AR configuration is locally evolving, namely whether a large helicity and magnetic winding are building up or not, and whether the current-carrying structure is building up or just the potential-field structure is continuing. In the case of minimum-phase storms, global toroid patterns evolve much faster than that in the peak phase; hence a close look at the sympathetic emergence and the buildup of their local dynamics is the best reliable signal that can be sent to prevent the hazardous impact of the unusual big storms during the minimum phase, despite having only just hours lead time.

In a future study, we will examine more peak-phase and minimum-phase storms to compare and build better statistics. Combining the evolutionary patterns of the global toroids in which the ARs are tightly stringed, along with the evolution of the local configuration of individual, flare-prolific ARs, the storms can be predicted with a significant lead time of several days. A natural question that should be answered is to whether the relationship between tipped-away regions of the toroid and strong helicity/winding input always holds or if such ARs can

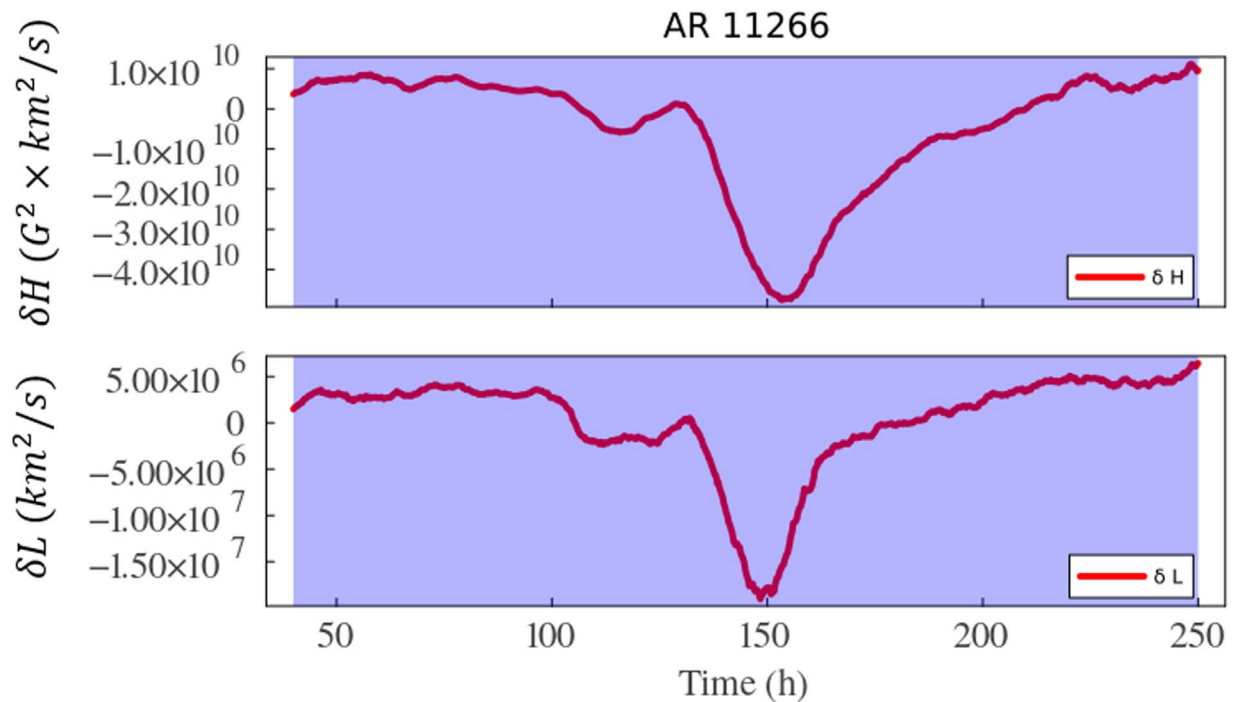


Figure 11. Evolution of the magnetic helicity imbalance (top) and magnetic winding imbalance (bottom) for AR 11266. Negative values indicate the injection of potential-dominated magnetic structure and positive values indicate current-carrying-dominated magnetic field structure.

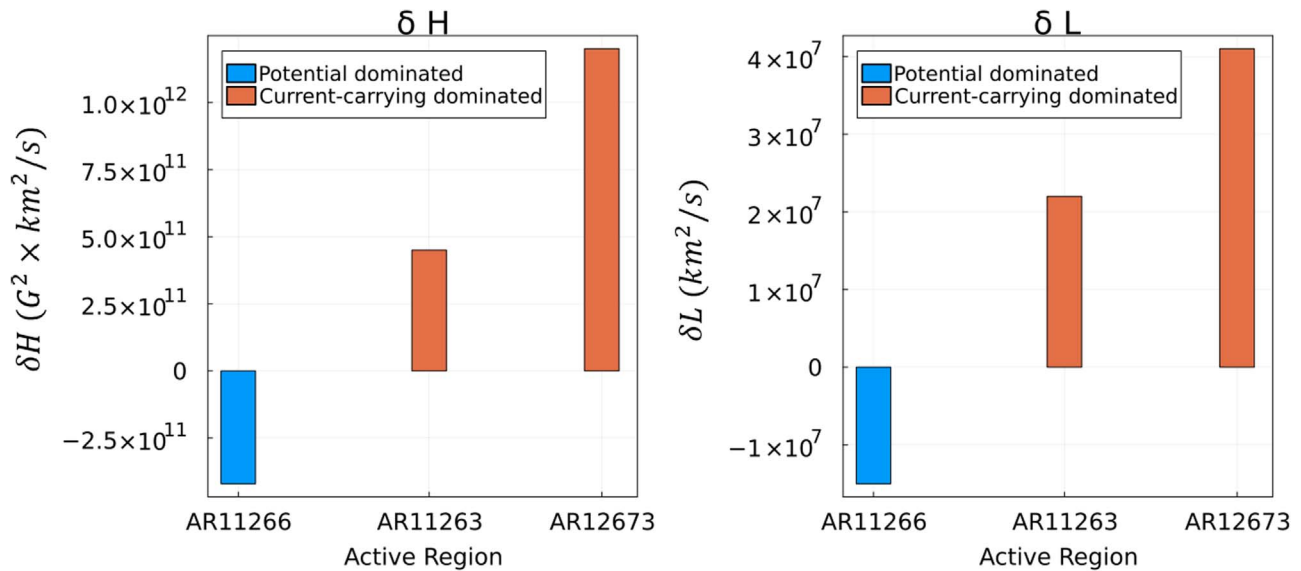


Figure 12. Summary of the maximal deviation of the helicity imbalance (left) and the magnetic winding imbalance (right).

also exist in longitudes where north and south toroids approach each other.

The analysis and derivation of pre-solar-storm features we presented here is very similar to the Earth's weather prediction from the troughs and ridges associated with Rossby waves, which provide the conditions for the formation of storms (Holton 1973). The analysis of atmospheric synoptic charts (Bluestein 1992) allowed meteorologists to predict the weather with the lead time of a few days. Similarly, our analysis suggests that solar storms can be predicted with one solar rotation lead time, meaning about one month lead time, if we can derive the prestorm features by utilizing information from

both the global toroid patterns in which flare-prone ARs manifest and their local dynamics.

Acknowledgments

This work is supported by the National Center for Atmospheric Research, which is a major facility sponsored by the National Science Foundation under cooperative agreement 1852977. We acknowledge support from several NASA grants, namely M.D. and B.R. acknowledge NASA-LWS award 80NSSC20K0355 and NASA-HSR award 80NSSC21K1676. M.D. also acknowledges COFFIES Phase II NASA-DRIVE Center for the subaward from Stanford with award number

80NSSC22M0162. A.N. acknowledges NASA-DRIVE Center COFFIES grant 80NSSC20K0602. A.S.W.T. has been supported by Fundação de Amparo à Pesquisa do Estado de São Paulo (FAPESP; grant 2020/14162-6). C.P. thanks UKRI/STFC for financial support through the consortium grant ST/W00108X/1. D.M. acknowledges support from an Innovation Placement supported by the DiRAC HPC Facility as part of the DiRAC Federation Project. Funding for the DiRAC Federation Project was provided by the URKI Digital Research Infrastructure programme. D.M., C.P., and B.R. welcome support from the US Air Force Office for Scientific Research (AFOSR): FA8655-20-1-7032.

Appendix

Potential and Current-carrying Helicity and Winding

Several works (Pariat et al. 2017; Raphaldini et al. 2022) have highlighted the importance not only of the total helicity for the understanding of the flaring activity in ARs, but also their decompositions in terms of potential and current-carrying components. If we define the current-carrying magnetic field as $\mathbf{B}_C = \mathbf{B} - \mathbf{B}_P$, then the following decompositions can be defined for the magnetic field foot-point motion:

$$\mathbf{u}(\mathbf{x}) = \mathbf{v}_{\parallel}(\mathbf{x}) - \frac{v_z}{B_z} \mathbf{B}_{\parallel c}(\mathbf{x}) - \frac{v_z}{B_z} \mathbf{B}_{\parallel p}(\mathbf{x}), \quad (\text{A1})$$

where $\mathbf{v}_{\parallel}(\mathbf{x})$ is the in plane component of the velocity, also known as “braiding-motion.” The current-carrying velocity is then defined as:

$$\mathbf{u}_c(\mathbf{x}) = \mathbf{v}_{\parallel}(\mathbf{x}) - \frac{v_z}{B_z} \mathbf{B}_{\parallel c}(\mathbf{x}), \quad (\text{A2})$$

while the potential component of the velocity is defined as:

$$\mathbf{u}_p(\mathbf{x}) = \mathbf{v}_{\parallel}(\mathbf{x}) - \frac{v_z}{B_z} \mathbf{B}_{\parallel p}(\mathbf{x}), \quad (\text{A3})$$

where the symbol \parallel detones the parallel component of the respective quantity. Finally, we define the current-carrying component of the helicity as:

$$H_c = \frac{1}{2\pi} \int_0^T \int_{\partial V} \int_{\partial V} B_z(\mathbf{x}) B_z(\mathbf{y}) \times \frac{(\mathbf{u}_c(\mathbf{x}) - \mathbf{u}_c(\mathbf{y})) \times (\mathbf{x} - \mathbf{y})}{|\mathbf{x} - \mathbf{y}|^2} d^2y d^2x dt, \quad (\text{A4})$$

and the potential component of the helicity as:

$$H_p = \frac{1}{2\pi} \int_0^T \int_{\partial V} \int_{\partial V} B_z(\mathbf{x}) B_z(\mathbf{y}) \times \frac{(\mathbf{u}_p(\mathbf{x}) - \mathbf{u}_p(\mathbf{y})) \times (\mathbf{x} - \mathbf{y})}{|\mathbf{x} - \mathbf{y}|^2} d^2y d^2x dt. \quad (\text{A5})$$

The respective densities of the injected current-carrying and potential helicities are defined as:

$$\mathcal{H}_c(\mathbf{x}) = \int_{\partial V} B_z(\mathbf{x}) B_z(\mathbf{y}) \frac{(\mathbf{u}_c(\mathbf{x}) - \mathbf{u}_c(\mathbf{y})) \times (\mathbf{x} - \mathbf{y})}{|\mathbf{x} - \mathbf{y}|^2} d^2y, \quad (\text{A6})$$

and:

$$\mathcal{H}_p(\mathbf{x}) = \int_{\partial V} B_z(\mathbf{x}) B_z(\mathbf{y}) \frac{(\mathbf{u}_p(\mathbf{x}) - \mathbf{u}_p(\mathbf{y})) \times (\mathbf{x} - \mathbf{y})}{|\mathbf{x} - \mathbf{y}|^2} d^2y. \quad (\text{A7})$$

Similar definitions hold for the magnetic winding. We define the current-carrying component of the winding as:

$$L_c = \frac{1}{2\pi} \int_0^T \int_{\partial V} \int_{\partial V} I_z(\mathbf{x}) I_z(\mathbf{y}) \times \frac{(\mathbf{u}_c(\mathbf{x}) - \mathbf{u}_c(\mathbf{y})) \times (\mathbf{x} - \mathbf{y})}{|\mathbf{x} - \mathbf{y}|^2} d^2y d^2x dt, \quad (\text{A8})$$

and the potential component of the winding as:

$$L_p = \frac{1}{2\pi} \int_0^T \int_{\partial V} \int_{\partial V} I_z(\mathbf{x}) I_z(\mathbf{y}) \times \frac{(\mathbf{u}_p(\mathbf{x}) - \mathbf{u}_p(\mathbf{y})) \times (\mathbf{x} - \mathbf{y})}{|\mathbf{x} - \mathbf{y}|^2} d^2y d^2x dt. \quad (\text{A9})$$




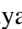



The respective densities the injected current-carrying and potential windings are defined as:

$$\mathcal{L}_c(\mathbf{x}) = \frac{1}{2\pi} \int_{\partial V} I_z(\mathbf{x}) I_z(\mathbf{y}) \frac{(\mathbf{u}_c(\mathbf{x}) - \mathbf{u}_c(\mathbf{y})) \times (\mathbf{x} - \mathbf{y})}{|\mathbf{x} - \mathbf{y}|^2} d^2y, \quad (\text{A10})$$

and:

$$\mathcal{L}_p(\mathbf{x}) = \frac{1}{2\pi} \int_{\partial V} I_z(\mathbf{x}) I_z(\mathbf{y}) \frac{(\mathbf{u}_p(\mathbf{x}) - \mathbf{u}_p(\mathbf{y})) \times (\mathbf{x} - \mathbf{y})}{|\mathbf{x} - \mathbf{y}|^2} d^2y. \quad (\text{A11})$$

ORCID iDs

Breno Raphaldini  <https://orcid.org/000-0002-0744-9746>
Mausumi Dikpati  <https://orcid.org/0000-0002-2227-0488>
Aimee A. Norton  <https://orcid.org/0000-0003-2622-7310>
Andre S. W. Teruya  <https://orcid.org/0000-0001-5113-7937>
Scott W. McIntosh  <https://orcid.org/0000-0002-7369-1776>
Christopher B. Prior  <https://orcid.org/0000-0003-4015-5106>
David MacTaggart  <https://orcid.org/0000-0003-2297-9312>

References

- Alielden, K., MacTaggart, D., Ming, Q., Prior, C., & Raphaldini, B. 2023, *RASTI*, **2**, 398
- Arnold, V. I., & Khesin, B. A. 2008, *Topological Methods in Hydrodynamics* (Berlin: Springer),
- Attié, R., Kirk, M. S., Thompson, B. J., Muglach, K., & Norton, A. A. 2018, *SpWea*, **16**, 1143
- Balthasar, H., & Schüssler, M. 1983, *SoPh*, **87**, 23
- Barnes, G., Leka, K., Schrijver, C., et al. 2016, *ApJ*, **829**, 89
- Berger, M. A., & Field, G. B. 1984, *JFM*, **147**, 133
- Biskamp, D. 2003, *Magnetohydrodynamic Turbulence* (Cambridge: Cambridge Univ. Press)
- Bluestein, H. 1992, *Synoptic-dynamic Meteorology in Midlatitudes: Volume 1, Principles of Kinematics and Dynamics* (New York: Oxford Univ. Press)
- Bobra, M. G., Sun, X., Hoeksema, J. T., et al. 2014, *SoPh*, **289**, 3549
- Boers, N. 2019, *Natur*, **875663**, 373
- Branch, M. A., Coleman, T. F., & Li, Y. 1999, *SJSC*, **21**, 1
- Cally, P. S., Dikpati, M., & Gilman, P. A. 2003, *ApJ*, **582**, 1190

- Cameron, R., Dikpati, M., & Brandenburg, A. 2017, *SSRv*, 210, 367
- Chae, J. 2001, *ApJL*, 560, L95
- Chae, J., Moon, Y.-J., & Park, Y.-D. 2004, *SoPh*, 223, 39
- Démoulin, P., & Pariat, E. 2009, *AdSpR*, 43, 1013
- Dikpati, M., Belucz, B., Gilman, P. A., & McIntosh, S. W. 2018a, *ApJ*, 862, 159
- Dikpati, M., Cally, P. S., McIntosh, S. W., & Heifetz, E. 2017, *NatSR*, 7, 14750
- Dikpati, M., & Gilman, P. A. 2009, *SSRv*, 144, 67
- Dikpati, M., Gilman, P. A., Guerrero, G. A., et al. 2022, *ApJ*, 931, 117
- Dikpati, M., & McIntosh, S. W. 2020, *SpWea*, 18, e02109
- Dikpati, M., McIntosh, S. W., Bothun, G., et al. 2018b, *ApJ*, 853, 144
- Dikpati, M., McIntosh, S. W., Chatterjee, S., et al. 2021, *ApJ*, 910, 91
- Dziembowski, W., & Kosovichev, A. 1987, *AcA*, 37, 341
- Gilman, P. A. 1968, *Sci*, 160, 760
- Gilman, P. A., & Fox, P. A. 1997, *ApJ*, 484, 439
- Green, L. M., Thalmann, J. K., Valori, G., et al. 2022, *ApJ*, 937, 59
- Gupta, M., Thalmann, J., & Veronig, A. 2021, *A&A*, 653, A69
- Harris, J., Dikpati, M., Hewins, I. M., et al. 2022, *ApJ*, 931, 54
- Hathaway, D. H. 2015, *LRSF*, 12, 1
- Hathaway, D. H., Upton, L. A., & Mahajan, S. S. 2022, *FrASS*, 9, 419
- Hindman, B. W., & Jain, R. 2022, *ApJ*, 932, 68
- Holton, J. R. 1973, *AmJPh*, 41, 752
- Hoskins, B. J., & Hodges, K. I. 2002, *JAtS*, 59, 1041
- Hoskins, B. J., & Ambrizzi, T. 1993, *JAtS*, 50, 1661
- Hoskins, B. J., & Valdes, P. J. 1990, *JAtS*, 47, 1854
- James, A. W., Valori, G., Green, L. M., et al. 2018, *ApJL*, 855, L16
- Jing, J., Tan, C., Yuan, Y., et al. 2010, *ApJ*, 713, 440
- Khodairy, S., Sharaf, M., Awad, M., Hamed, R. A., & Hussein, M. 2020, *JPhCS*, 1523, 012010
- Korsós, M. B., Dikpati, M., Erdélyi, R., Liu, J., & Zuccarello, F. 2023, *ApJ*, 944, 180
- Kusano, K., Iju, T., Bamba, Y., & Inoue, S. 2020, *Sci*, 369, 587
- Kusano, K., Maeshiro, T., Yokoyama, T., & Sakurai, T. 2002, *ApJ*, 577, 501
- Kusano, K., Maeshiro, T., Yokoyama, T., & Sakurai, T. 2004, *ApJ*, 610, 537
- Leka, K., Park, S.-H., Kusano, K., et al. 2019a, *ApJS*, 243, 36
- Leka, K., Park, S.-H., Kusano, K., et al. 2019b, *ApJ*, 881, 101
- Liu, Y., Welsch, B. T., Valori, G., et al. 2023, *ApJ*, 942, 27
- Löptien, B., Gizon, L., Birch, A. C., et al. 2018, *NatAs*, 2, 568
- MacTaggart, D., & Prior, C. 2021, *GApFD*, 115, 85
- MacTaggart, D., Prior, C., Raphaldini, B., Romano, P., & Guglielmino, S. 2021, *NatCo*, 12, 6621
- Madden, R. A. 1979, *RvGeo*, 17, 1935
- McIntosh, S. W., Cramer, W. J., M., M. P. M., & Leamon, R. 2017, *NatAs*, 1, 0086
- Metcalf, T. R., Leka, K., & Mickey, D. 2005, *ApJL*, 623, L53
- Moon, Y.-J., Chae, J., Choe, G., et al. 2002, *ApJ*, 574, 1066
- Moraitis, K., Sun, X., Pariat, É., & Linan, L. 2019, *A&A*, 628, A50
- Neugebauer, M., Smith, E., Ruzmaikin, A., Feynman, J., & Vaughan, A. 2000, *JGR*, 105, 2315
- Pariat, E., Démoulin, P., & Berger, M. A. 2005, *A&A*, 439, 1191
- Pariat, E., Valori, G., Linton, M., Zuccarello, F., & Dalmasse, K. 2017, *A&A*, 601, A125
- Park, S.-H., Leka, K., Kusano, K., et al. 2020, *ApJ*, 890, 124
- Pesnell, W. D. 2016, *SpWea*, 14, 10
- Prior, C., & MacTaggart, D. 2020, *RSPSA*, 476, 20200483
- Raphaldini, B., Dikpati, M., & McIntosh, S. W. 2023, *ApJ*, 953, 156
- Raphaldini, B., Medeiros, E., Raupp, C. F. M., & Teruya, A. S. 2020, *ApJL*, 890, L13
- Raphaldini, B., Prior, C. B., & MacTaggart, D. 2022, *ApJ*, 927, 156
- Raphaldini, B., & Raupp, C. F. 2015, *ApJ*, 799, 78
- Raphaldini, B., Teruya, A. S., Raupp, C. F., & Bustamante, M. D. 2019, *ApJ*, 887, 1
- Regnier, S., & Priest, E. 2007, *ApJL*, 669, L53
- Romano, P., Zuccarello, F. P., Guglielmino, S. L., & Zuccarello, F. 2014, *ApJ*, 794, 118
- Rosby, C.-G. 1939, *JMR*, 2, 38
- Rüdiger, G., & Brandenburg, A. 1995, *A&A*, 296, 557
- Schuck, P. W. 2008, *ApJ*, 683, 1134
- Silva, S., Lennard, M., Verth, G., et al. 2023, *ApJL*, 948, L24
- Simpson, J. J. 2011, *JGRA*, 116, A1130
- Sun, X., & Norton, A. A. 2017, *RNAAS*, 1, 24
- Sutcliffe, R. 1947, *QJRMS*, 73, 370
- Teruya, A. S., Raphaldini, B., & Raupp, C. F. 2022, *FrASS*, 9, 856912
- Thalmann, J., Inhester, B., & Wiegmann, T. 2011, *SoPh*, 272, 243
- Thalmann, J. K., Pietarila, A., Sun, X., & Wiegmann, T. 2012, *AJ*, 144, 33
- Thomson, N. R., Rodger, C. J., & Dowden, R. L. 2004, *GeoRL*, 31, L06803
- Vanselow, K. H. 2020, *IJAsB*, 19, 413
- Vemareddy, P. 2019, *ApJ*, 872, 182
- Zaqarashvili, T. V., Carbonell, M., Oliver, R., & Ballester, J. L. 2010a, *ApJ*, 709, 749
- Zaqarashvili, T. V., Carbonell, M., Oliver, R., & Ballester, J. L. 2010b, *ApJL*, 724, L95